ACS Catalysis

pubs.acs.org/acscatalysis

Research Article

Standardizing OER Electrocatalyst Benchmarking in Aqueous Electrolytes: Comprehensive Guidelines for Accelerated Stress Tests and Backing Electrodes

Matej Zlatar,* Daniel Escalera-López, Miquel Gamón Rodríguez, Tomáš Hrbek, Carina Götz, Rani Mary Joy, Alan Savan, Hoang Phi Tran, Hong Nhan Nong, Paulius Pobedinskas, Valentín Briega-Martos, Andreas Hutzler, Thomas Böhm, Ken Haenen, Alfred Ludwig, Ivan Khalakhan, Peter Strasser, and Serhiy Cherevko*

Cite This: *ACS Catal.* 2023, 13, 15375−15392

Read Online

ACCESS | Metrics & More | Article Recommendations | Supporting Information

ABSTRACT: The scarcity of iridium, needed to catalyze the sluggish oxygen evolution reaction (OER), hinders large-scale hydrogen production with proton exchange membrane water electrolyzers (PEMWEs). Crucial steps require reducing its loading while improving its overall activity and stability. Despite knowledge transfer challenges, cost and time constraints still favor aqueous model systems (AMSs) over real devices for the OER electrocatalyst testing. During AMS testing, benchmarking strategies such as accelerated stress tests (ASTs) aim at improving catalyst lifetime estimation compared to constant current loads. This study systematically evaluates a commercial Ir catalyst by modifying both AST parameters and the employed backing electrodes to examine their impact on activity−stability relationships. A comprehensive set of spectroscopy and microscopy techniques, including in situ inductively coupled plasma mass spectrometry, is employed to monitor Ir and backing electrode modifications. Our findings demonstrate that the choice of both lower potential limit (LPL) in ASTs and backing electrode significantly influences the estimation of Ir-based electrocatalysts' activity and stability. Unique degradation mechanisms, such as passivation, redeposition on active sites, and contribution to the OER, were observed for different backing electrodes at varying LPLs. These results emphasize the importance of optimizing parameters and electrode selection in ASTs to accurately assess the electrocatalyst performance. Furthermore, they establish the foundation for developing relevant standardized test protocols, enabling the cost-effective development of high-performance catalysts for PEMWE applications.

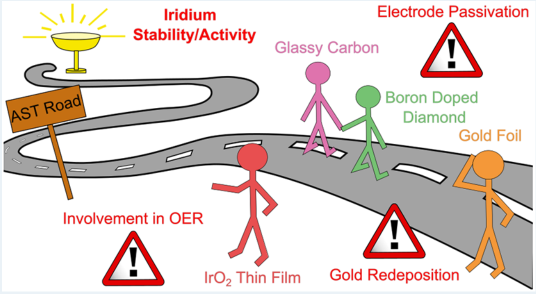

KEYWORDS: *oxygen evolution reaction, iridium, accelerated stress test, dissolution, glassy carbon, boron-doped diamond, gold*

1. INTRODUCTION

Green hydrogen, produced via water electrolysis, has the potential to significantly transform the energy sector worldwide by promoting sustainable, carbon-neutral energy storage.[1] This promising energy carrier can help address the intermittency issues associated with renewable energy sources, which currently pose major challenges to achieving the European Climate Law's goal of climate neutrality by 2050 and a 55% net greenhouse gas emission reduction until 2030 (compared to 1990 levels).[2] Despite hydrogen's favorable characteristics, such as high energy density, low chemical complexity, and high efficiency, the current production of hydrogen from renewable electricity sources remains relatively low, accounting for less than 1% of the total hydrogen production globally. In comparison, water electrolysis contributes only about 4%.[3]

In recent years, proton exchange membrane water electrolyzers (PEMWEs) have gained attention as a promising technology for large-scale hydrogen production. Unlike traditional alkaline electrolyzers, which lack dynamic operation capabilities required for direct coupling to fluctuating energy sources, PEMWEs offer operation at high current densities and variable power input, high efficiency, and a fast rate of H_2 production. Moreover, while anion exchange membrane water electrolyzers (AEMWEs) show potential, they have not yet reached a technology readiness level suitable for upscaling. As a result, PEMWEs are currently considered the preferred system for upscaling.

The successful deployment of PEMWEs still depends on resolving several key technical challenges, including the demanding acidic conditions and high potentials at the anode

Received: August 17, 2023
Revised: October 19, 2023
Accepted: October 24, 2023
Published: November 13, 2023

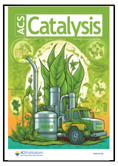

side, where the sluggish oxygen evolution reaction (OER) takes place. Highly active and stable electrocatalysts based on noble metals, such as iridium (Ir) and ruthenium (Ru), are required to drive this reaction efficiently.[4] While the current cost of these materials does not pose a significant barrier to their use in PEMWEs, the challenges associated with scaling up the technology to the gigawatt and terawatt levels necessitate a more cost-effective solution.[5−7] Also, current hydrogen pricing obtained from renewable water electrolysis is 4 \$/kg H_2,[8] far beyond the hydrogen price target set by the United States Department of Energy (DoE) (1\$/kg H_2).[9] Furthermore, a completely decarbonized mobility sector would require the current Ir-normalized specific power density to be reduced 50-fold (from ∼0.5 to 0.01 g_{Ir} kW^{-1}), followed by an increased Ir ore mining capacity.[5,10] As a result, there is a growing focus on reducing the noble metal content in PEMWE anodes and developing more stable and effective catalysts that can deliver high performance and longevity while being cost-effective and being produced at scale to reach such targets.

The development and testing of alternative electrocatalysts represents a significant research challenge, slowing progress in PEMWE commercialization. On the one hand, testing of activity and stability of electrocatalysts in real devices is desirable but prohibitively expensive and time-consuming. On the other hand, alternative aqueous model systems (AMSs), typically used in laboratory studies, are hindered by the absence of standard testing procedures to model electrocatalyst behavior in PEMWEs. Indeed, transferring knowledge gained from AMSs to real devices is still not trivial due to the higher complexity and differences in electrolytes used in PEMWEs compared to AMSs. While AMSs use liquid acidic electrolytes, PEMWEs employ solid polymer electrolytes and ionomers with deionized water.[11,12] Although the benchmarking of Ir catalysts for OER electrocatalysis is predominantly performed in AMSs, recent studies have demonstrated a clear discrepancy in catalyst lifetimes between AMSs and PEMWEs.[13,14] With this in mind, new electrocatalyst benchmark strategies and more realistic test protocols must be developed to estimate the catalyst lifetime more accurately.

Considering relatively recent literature, evaluating catalyst performance over a 2 h test with a constant current density hold of 10 mA cm^{-2} was proposed in a series of studies, aiming to correlate the device performance with the solar-to-fuel conversion efficiency of 10% under 1 sun illumination.[15,16] Later on, accelerated stress tests (ASTs) were introduced as a time-efficient method to simulate long-term operation in real devices.[17,18] ASTs offer the advantage of shorter testing duration while simulating performance over extended periods, including fluctuating input power in PEMWEs.[19] The development of ASTs,[20] particularly transient ASTs using potential square-wave cycles in three-electrode setups, has shown promise in providing representative degradation rates compared to PEMWEs.[21] However, the AST protocol remains an important parameter that requires a thorough evaluation as it can significantly impact the obtained stability metrics. Prior studies have examined the impact of the upper potential limit (UPL) of ASTs in half-cell tests[22] and the effect of the lower voltage limit in membrane electrode assemblies (MEAs).[23] Both studies have highlighted the potential impact of these parameters on the degradation of the Ir performance. However, additional research is required to gain a more comprehensive understanding of their effects.

Highlighting the accumulation of oxygen bubbles within the catalyst layer and its interface with the electrolyte during the OER in AMS has become crucial as well, particularly given its recent increase in attention.[12] Bubble accumulation, hypothesized to obstruct electrolyte access to the catalyst surface, may diminish the active surface area, increase overpotential, and potentially impact catalyst dissolution rates.[24,25] Consequently, bubble accumulation is often and mistakenly perceived as catalyst degradation and is claimed as a primary cause of stability discrepancy between MEA and AMS.[24,26] Previously, it was demonstrated that a 30 min Ar gas purge at open-circuit potential (OCP) can partially reverse OER activity decay caused by microbubbles.[24] Additionally, using ultrasonication in the rotating disk electrode (RDE) setup stabilized overpotential during galvanostatic holds, further confirming the detrimental role of microscopic bubbles in the performance decay.[27]

In response to these issues, two alternative setups were proposed. Petzoldt et al. successfully applied catalyst-coated membranes in a modified RDE method (MRDE), distinguishing between reversible and irreversible degradation through effective macroscopic bubble removal.[28] On the other hand, Podboršek et al. introduced a modified floating electrode setup and dynamic protocol that integrated OCP and OER intervals, efficiently managing bubbles and correlating low oxidation tendency with surface roughening as the predominant degradation mechanisms.[29]

Newly synthesized Ir-based and alternative catalysts are commonly produced in powder form, necessitating their dispersion as an ink formulation and subsequent preparation on a backing electrode using the drop-casting method. Selecting an appropriate backing electrode for testing poses challenges as it should ideally be inert, electrically conductive, and exhibit chemical and thermal stability. However, finding a backing electrode that demonstrates no electrochemical activity under the test conditions for the active electrocatalyst is complex and often poorly understood. Real-world complexity arises as there is no perfect backing electrode, and it can contribute to electrochemical measurements through capacitance, surface phase changes, or background electrocatalysis. Therefore, the choice of the backing electrode should closely mimic inert behavior under specific testing conditions or undergo a comprehensive investigation to understand its influence. However, studying the electrochemical reactivity of a substrate itself can be problematic as it depends not only on its inherent properties but also on factors such as the electrolyte, potential range, temperature, gas purge, and tested electrocatalyst.

The available literature on selecting backing electrodes, particularly for the OER, remains scarce. Benck et al. previously contributed to this area by investigating the inert potential windows of various backing electrode materials and providing recommendations for suitable materials based on different experimental conditions.[30] Geiger et al. conducted a study that sheds light on the limitations of drawing conclusions about Ir stability based solely on electrochemical measurements, particularly when considering overpotential changes during galvanostatic holds. Their research, employing an online inductively coupled plasma mass spectrometer (online ICP−MS) setup, revealed that backing electrode materials such as glassy carbon (GC) can undergo passivation and mask the degradation phenomena of the electrocatalyst. Additionally, they explored alternative backing electrode materials such as gold and boron-doped diamond (BDD), recommending their use for short accelerated aging investigations in OER.[31] Yi et al. conducted a study to investigate the chemical resistance of GC under electrochemically oxidative conditions, specifically during the OER in an acidic environment. Through spectroscopic analysis, they demonstrated that the degradation of the GC electrode in acidic media occurs through surface oxide formation via an acid-catalyzed process, resulting in ring opening in the graphitic structure and subsequent bulk oxidation.[32] Another study also investigated the electrochemical oxidation of GC in acidic media, revealing structural changes at the surface in contact with the electrolyte, and proposed a structural decomposition mechanism. The study also observed an increase in the concentration of oxygen functional groups with increasing applied potential.[33] In a more recent study, an increased catalyst loading was found to improve the stability of the GC electrode. Since catalyst dissolution was not the main degradation mechanism within the studied time scales, the researchers proposed that increased catalyst loading hinders the mass transfer of the electrolyte to the GC surface and serves as an oxidative current sink during the OER, protecting the GC electrode and slowing substrate surface oxidation.[34]

Despite ongoing research into the passivation of the GC electrode, it remains a prevalent choice in the OER community mostly due to its good electrical conductivity and affordability. While Au has been suggested as an alternative[31] and is another commonly used backing electrode,[22,35] it has limitations. Notably, Au is more expensive than GC and has been demonstrated to dissolve at high positive potentials, starting at ca. 1.3 V_{RHE} and accelerating at ca. 1.8 V_{RHE} or higher.[36,37] Moreover, we also note the use of a Pt backing electrode, as previously employed by Lončar et al.[38] Au and Pt differ in their dissolution. Thus, under potentiodynamic conditions, the onset potential for anodic dissolution of Pt (~0.95 V_{RHE}) is lower compared to Au (~1.25 V_{RHE}).[4,37,39] In contrast, under more quasi-steady-state conditions in the OER region, Pt forms a passive oxide film, protecting it from further dissolution. Meanwhile, the steady-state dissolution of Au during the OER is significantly higher compared to its transient dissolution seen during initial oxide formation at lower potentials. Hence, when utilizing these backing electrodes, the potential influence of Pt on the measured OER activity of the tested catalysts should be carefully considered as well as the intense dissolution of Au. All things considered, the Pt as a potential backing electrode for the OER necessitates further detailed investigation.

Considerable research has been conducted in this field; however, there is still a gap in understanding the impact of ASTs on different backing electrodes. Additionally, a more comprehensive and systematic experimental study of all potential backing electrodes is required to develop guidelines for selecting suitable ones. Among the potential options, the previously proposed BDD[31] and the recently explored polycrystalline Ir electrode[27] are noteworthy. Notably, despite its intrinsic OER activity, the Ir backing electrode differs from other backing electrodes by effectively preventing the formation of additional contact resistance between the catalyst layer and the backing electrode substrate as a result of passivation. Furthermore, it has been demonstrated that IrO_2 thin films exhibit exceptional stability even under significant cathodic[40] and anodic polarizations.[41]

Therefore, in this study, we systematically evaluated the stability of a commercial Ir black catalyst, which is representative for the PEMWE application, under various AST parameters and backing electrodes: GC, Au foil, BDD, and an IrO_2 thin film. By using an electrochemical scanning flow cell (SFC) coupled to ICP−MS (SFC-ICP-MS), Raman spectroscopy, X-ray photoelectron spectroscopy (XPS), and scanning and transmission electron microscopy (SEM and TEM), our findings reveal the critical role of lower potential limits (LPLs) and backing electrode selection in determining catalyst activity and stability. By optimizing these parameters, we demonstrate that more accurate performance assessments of Ir-based electrocatalysts can be achieved, paving the way for the development of high-performance, cost-effective catalysts for PEMWE applications.

2. EXPERIMENTAL SECTION

2.1. Thin-Film Materials. Thin films of boron-doped nanocrystalline diamond (BDD) were deposited using microwave plasma-enhanced chemical vapor deposition in the ASTeX 6500 series reactor. 150 nm thick BDD thin films were grown in 2 h on polished single crystal (100) silicon substrates (7 mm × 7 mm) at a temperature of 725 °C. For more detailed information about the procedure, the reader is referred to our previous publication.[42] Metallic Ir thin films were magnetron sputtered by PVD on 100 mm diameter, single-side polished (100) Si wafers with a 500 nm wet thermal SiO_2 barrier layer. Depositions were carried out in a loadlocked UHV chamber having a confocal cathode to substrate configuration (CMS 600/400 LIN, DCA Instruments, Finland), using substrate rotation to achieve better than 1% thickness uniformity. The 100 mm diameter Ir target (Evochem, 99.99% purity) was sputtered with 90 W DC in 0.67 Pa of Ar (99.9999% purity) on a 15 nm Ti (Sindlhauser, 99.99%) adhesion layer deposited immediately prior at 25 °C without additional intentional heating. The samples were heat-treated at 600 °C in a tube furnace for 10 h in an oxygen atmosphere to obtain rutile IrO_2.

2.2. Powder Materials. For the SFC-ICP-MS stability measurements, the iridium black powder (Alfa Aesar) was dispersed in a 7:1 ratio of H_2O [Merck, Mili-Q IQ 7000, 18 MΩ, total organic carbon < (TOC) < 3 ppb] and isopropanol (Emsure, Merck, ≥99.8% purity). Potential catalyst detachment was minimized by adding Nafion ionomer solution (D-520, Sigma-Aldrich, 5 wt %) as a binder (catalyst ionomer weight ratio of 4:1). The mixture was sonicated in an ice bath with a horn sonicator (Branson Ultrasonics SFX150) for 15 min (4 s/2 s on/off pulses). After sonication, the pH was adjusted to ~11 with 1 M KOH before drop-casting 0.2 μL suspension (0.66 mg/mL) on GC (5 × 5 cm^2, Sigradur G, HTW), Au foil plates (25 × 25 mm, 99.95%, Alfa Aesar), and the as-received IrO_2 and BDD thin films. Depending on the size of the catalyst ink spots, evaluated with a Keyence VK-X250 profilometer, the estimated catalyst loading was ~10 $\mu g_{cat}\ cm^{-2}$, while the spot thickness was ~100 nm.

A similar ink preparation method was used in the RDE measurements. The H_2O and isopropanol ratio was adjusted to 3:1, and the catalyst/Nafion ionomer weight ratio was adjusted to 2:1. To achieve the total iridium loading of ~32 $\mu g_{cat}\ cm^{-2}$, the 10 μL ink aliquots of 0.32 mg/mL ink were drop-cast twice (drying step in between) on Au and GC RDE tips with a surface area of 0.1963 cm^2 (Pine Research), rotating at 200 rpm.

2.3. Physical Characterization. XPS measurements were performed using an EnviroESCA system (SPECS Surface Nano Analysis, GmbH Germany) equipped with a monochromated Al K_α X-ray source (1486.6 eV) and hemispherical analyzer (Specs PHOIBOS) operating under ultrahigh vacuum conditions (10^{-9} mbar). The core-level spectra of C 1s, O 1s, B 1s, and Ir 4f were recorded with a pass energy of 20 eV, a step size of 0.1 eV, and a dwell time of 0.3 s. The measured XPS spectra were processed using KolXPD software (Kolibrik.net, Czech Republic).

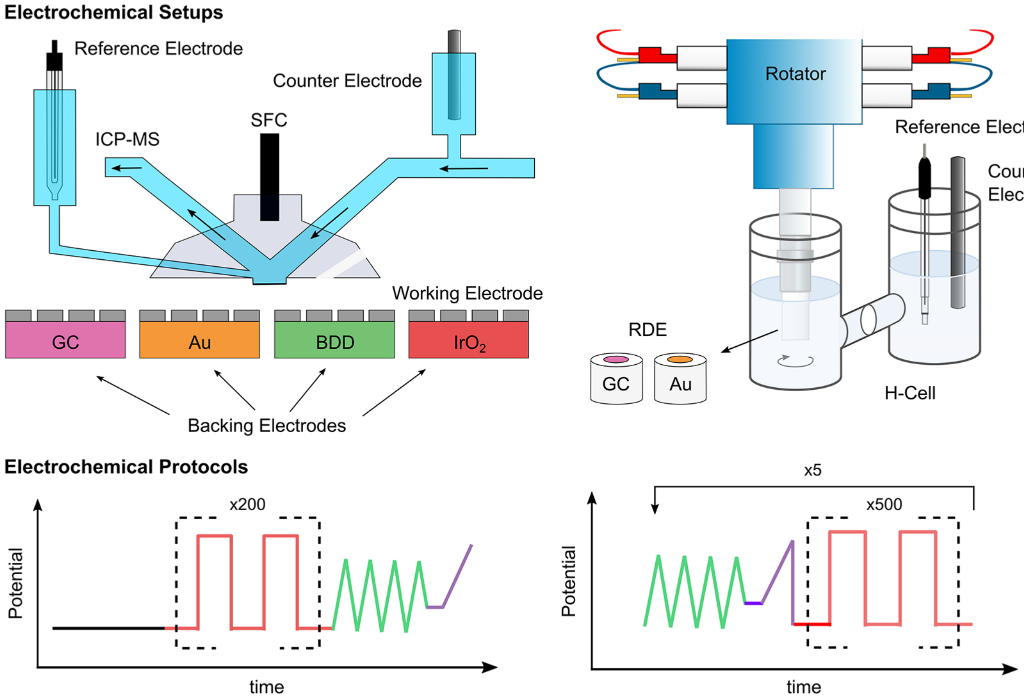

Figure 1. Simplified illustration of the SFC and RDE setups and electrochemical protocols employed in the study. The SFC-ICP-MS setup and protocol are shown on the left, while the RDE setup and protocol are displayed on the right. In both protocols, CVs are represented in green, LSVs in purple, and the ASTs used in the protocols are represented in red.

The Raman spectra were obtained using a WITec alpha 300 RA confocal Raman microscope. A 532 nm solid-state laser at a power of 5 mW was focused onto the sample with a ZEISS LD EC Epiplan-Neofluar 50×/0.55 objective. The scattered light was analyzed with a WITec UHTS 300 VIS spectrometer with a Peltier-cooled back-illuminated EMCCD camera (1600 pixel) and a 600 grooves/mm optical grating. For each sample, the Raman spectra were acquired at five different positions. Five single spectra were accumulated per position with an integration time of 0.5 s per spectrum. The shape-based background subtraction algorithm from WITec project FIVE+ software was used at a shape size of 400 to remove the fluorescent background of the samples.

The morphology was examined using a MIRA 3 (Tescan) scanning electron microscope operated with an electron beam energy of 10 keV and a Talos F200i (S)TEM (Thermo Fisher Scientific) operated at 200 keV. The elemental composition and mapping of the samples were determined by energy-dispersive X-ray spectroscopy (EDX) using an XFlash 6-10 detector (Bruker) integrated into the SEM.

2.4. Stability Measurements (SFC-ICP-MS). The detection of dissolved metal ions during electrochemical measurements was achieved by coupling the SFC outlet online with ICP−MS. The Ar-purged 0.05 M H_2SO_4 electrolyte was prepared prior to each measurement by diluting concentrated H_2SO_4 (Suprapure 96%, Merck) with ultrapure water (18.2 MΩ cm, TOC <3 ppb). The electrolyte was pumped from a reservoir through the SFC and mixed with an internal standard (1:1 ratio) by an ICP−MS peristaltic pump at a constant flow rate of ~3.5 μL/s. The counter electrode (graphite rod, 5 mm, HTW Sigradur G) and the reference electrode (Ag/AgCl, Metrohm, Germany) were placed at the SFC inlet and outlet, respectively. The working electrode, prepared by drop-casting ink spots on the backing electrodes (described in the previous section), was placed on the XYZ position stage and approached from the top with an SFC opening (0.033 cm^2). All electrodes were connected to a VSP-150 potentiostat (Biologic), and the measured potentials were calibrated and reported versus the reversible hydrogen electrode (RHE) scale. The ICP−MS instruments, PerkinElmer NexION 350X and 300X (PerkinElmer), were optimized daily and calibrated with solutions of 0.5, 1, and 5 ppb of the investigated elements (CertiPUR ICP−MS Standard, Merck), diluted from 1000 ppm. Potential instrument drifts, matrix effects, and polyatomic interferences were monitored by adding a 10 ppb internal standard solution of ^{187}Re (CertiPUR ICP−MS Standard, Merck), which has a similar mass and first ionization potential as ^{193}Ir. A detailed description of the SFC-ICP-MS setup has been provided in our previous publications.[43,44]

2.5. Electrochemical Measurements (RDE). Long-term ASTs were carried out using a classical three-electrode setup in the H-cell (Pine Research), connected to the RDE setup [Modulated Speed Rotator (MSR), Pine Research]. The reference electrode and the counter electrode (see previous section) were separated from the working electrode to avoid contamination by Cl^- ions and the redeposition of Ir ions on the counter electrode. The working electrode consisted of drop-cast Ir black powder on GC and Au disks (Ø ≈ 5 mm, Pine Research) embedded in poly(tetrafluoroethylene) (PTFE). Before each experiment, the GC and Au disks were mirror-polished with a 0.05 μm alumina suspension. The H-cell was filled with 0.05 M H_2SO_4 electrolyte diluted from concentrated H_2SO_4 (Suprapure 96%, Merck) and purged with argon gas for 30 min before each experiment. A rotation speed of 1600 rpm was maintained, while the potential was controlled with a VSP-150 potentiostat (Biologic). The ohmic resistance was measured by impedance spectroscopy as a high-frequency interception of the Re (Z) axis and was used to compensate for the iR drop during each AST.

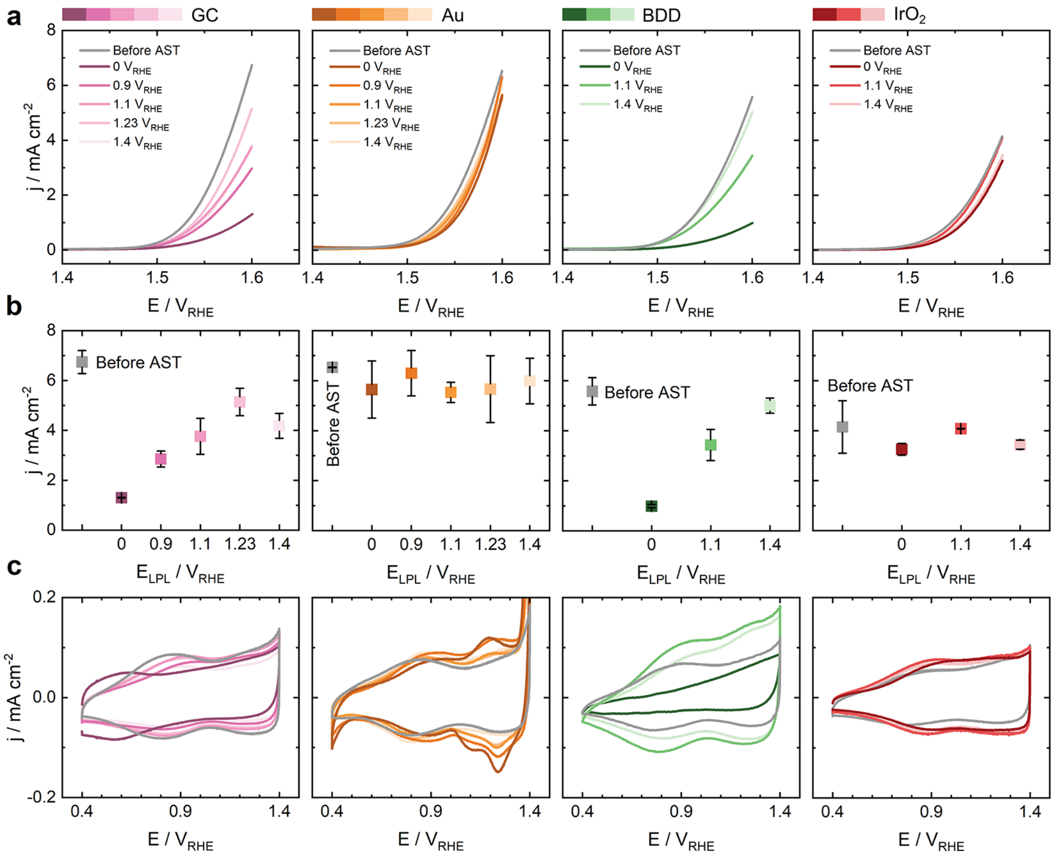

Figure 2. AST-induced changes of Ir electrochemistry at different LPLs as measured by SFC. (a) OER activity assessment of Ir black on different backing electrodes: GC (purple), Au (orange), BDD (green), and IrO_2 (red). LSV potential window: 1.2 to 1.6 V_{RHE}, scan rate: 10 mV s^{-1}. (b) OER geometric current densities of Ir black at 1.6 V_{RHE}, based on the LSVs shown in (a). Each data point represents an average of at least two independent measurements. (c) CVs of Ir black, obtained using a scan rate of 50 mV s^{-1}. Only the last cycle out of four is presented when the steady state is achieved. Electrolyte: 0.05 M H_2SO_4.

2.6. Electrochemical Protocols. Linear sweep voltammetry (LSV) was measured in the potential range from 1.1 to 1.6 V_{RHE}, with a scan rate of 10 mV s^{-1}. Cyclic voltammograms (CVs) were measured in the potential range of 0.4 V_{RHE} < E < 1.4 V_{RHE}, with a scan rate of 50 mV s^{-1}. Only the last of four cycles, when the steady-state was achieved, is shown. Electrochemical impedance spectroscopy (EIS) measurements were performed at a potential of 1 V_{RHE}, employing a sinusoidal signal with a 10 mV amplitude in the frequency range from 100 kHz to 500 mHz. The ohmic resistance was determined at the highest frequency intersection of the real axis.

In order to ensure reproducibility of the results, all measurements were repeated at least twice on individual pristine drop-cast catalyst spots. Differences in surface areas were accounted for by normalizing the absolute currents with the geometric surface area of the catalyst spots employed as working electrodes. The intrinsic activity was determined by normalizing the absolute currents using the average of integrated anodic and cathodic charges obtained from the CV within the range from 0.4 to 1.4 V_{RHE}. For more details on electrochemical protocols, see the Supporting Information provided.

3. RESULTS AND DISCUSSION

In order to accurately benchmark newly synthesized, advanced Ir, Ir-based, and non-Ir alternative OER catalysts, it is crucial to clearly distinguish between the degradation of the catalyst layer and that of the backing electrode during AST. If not properly understood, it can result in inaccurate conclusions, underestimating or overestimating the catalyst's performance and degree of degradation. To address this concern, a set of testing protocols was developed. First, we utilized an SFC-ICP-MS setup for quick screening of the influence of the potential protocol and backing electrode on Ir dissolution. Next, Ir dissolution and OER activity data were compared with those obtained in an extended AST with higher Ir loading samples on preselected backing electrodes in the RDE setup. As our catalyst, we chose commercially available Ir black, widely used as a benchmark material.[31,35,45,46] To evaluate their activity and stability, GC, Au, BDD, and IrO_2 backing electrodes were used. The schematic representation of the electrochemical setups and protocols used in the study is illustrated in Figure 1.

Both protocols incorporated several key steps, including four CV scans to detect any catalyst changes and determine the electrochemically active surface area (ECSA), as well as LSV to evaluate activity. Both were tested before and after the AST as the quality of the catalyst layer can influence its OER performance.[31,47] Figure S1 visually represents the thickness of drop-cast spots on different backing electrodes, as determined through laser profilometry measurements. The results demonstrate that the thickness of these spots consistently falls within a similar range of approximately 100 nm. Additionally, a consistent coffee ring pattern is observed. As a result, the influence of catalyst spot quality on different backing electrodes on the Ir performance can be disregarded.

The AST followed a methodology previously proposed[17,21] for simulating long-term MEA operation and testing OER, consisting of 3 s pulses with an UPL of 1.6 V_{RHE}. To avoid issues such as intense macroscopic bubble formation blocking active sites and higher dissolution rates, we did not test potentials higher than 1.6 V_{RHE} in this study. We note here that real *iR* drop-corrected potentials on Ir are comparable to those in real PEMWEs with high catalyst loading and high activity. Additionally, the effect of the UPL had been previously investigated.[22] Consequently, our focus shifted to studying LPLs, which play a crucial role in simulating realistic fluctuating electrolyzer operation when coupled with renewables. An LPL value close to the OCP in an MEA was initially examined, starting from 1.4 V_{RHE}.[48] Given the potential oxidation of backing electrodes at these values, various LPLs lower than 1.4 V_{RHE} were also tested, specifically 1.23, 1.1, and 0.9 V_{RHE}. Furthermore, 0 V_{RHE} was employed to simulate the effect of H_2 crossover in an MEA.[49,50] Each LPL value was associated with a distinct protocol evaluated in both the SFC-ICP-MS and RDE setups. In the SFC-ICP-MS setup, the AST was limited to 200 pulses due to setup limitations. On the other hand, in the RDE setup, the complete protocol with 500 pulses was repeated five times, resulting in a total of 2500 pulses. After every set of 500 pulses, activity and ECSA measurements were performed. Lastly, since the manuscript primarily focuses on the commonly used backing electrodes GC and Au, the BDD and IrO_2 backing electrodes were tested with only 0, 1.1, and 1.4 V_{RHE} LPLs, representing the most characteristic cases. For more details regarding the electrochemical protocol, the readers are referred to the Experimental Section 2.6 of the manuscript.

The following Results and Discussion chapter of this manuscript is structured into five main sections. In the first section, we evaluate the OER activity and changes in the CV of Ir black on various backing electrodes. In order to explain the observed differences, in the second section, we compare the stability of the catalyst. In the third section, we employ various surface characterization techniques to examine the condition of the backing electrodes before and after AST, shedding light on their degradation mechanisms. In the fourth section, we investigate the influence of an extended AST protocol combined with a higher Ir loading using the RDE setup. Finally, in the fifth section, we compare the Ir-specific OER activities on all backing electrodes after the AST.

3.1. Ir OER Activity in Relation to Different LPLs and Backing Electrodes.

In our investigation of the performance of Ir black, we followed a systematic approach. Initially, we prepared the ink and drop-cast it onto GC, Au, BDD, and IrO_2 thin-film electrodes. Using the drop-casting method, we ensured uniform deposition of the Ir black catalyst layer, establishing consistent starting conditions for the OER measurements. Using SFC-ICP-MS, we evaluated the OER performance by following the electrochemical protocol shown in Figure 1, which involved employing different LPLs.

Figure 2a showcases the OER activity of drop-cast Ir black, measured by LSV, in relation to the LPL applied during the AST protocol shown in Figure 1 (SFC) across the four backing electrodes. For enhanced clarity, Figure 2b also displays the corresponding current densities at 1.6 V_{RHE} extracted from the LSV measurements.

Before the AST, the OER activity of Ir black across the various backing electrodes was overall in good agreement. However, the activity was slightly lower on the BDD and IrO_2 electrodes, which can be attributed to higher contact resistance between the catalyst layer and the electrodes[31] or the lower in-plane conductivity of both BDD and IrO_2 thin films. Note that these data are not *iR* drop corrected as EIS measurements can influence the degradation and hence were excluded from these measurements. Furthermore, the low-surface area of catalyst spots (approximately 0.015 cm^2) in the SFC typically yields absolute currents in the μA and nA range, leading to a negligible *iR* drop. Following the AST, Ir activity changed across all backing electrodes and LPLs, although the impact was less pronounced on the Au and IrO_2 electrodes. The changes in Ir activity during the AST can be seen in Figure S2a, which shows significant variations in the OER activity of Ir black on GC and BDD, depending on the LPL. This variation in the OER activity may be attributed to the specific LPL hold before the AST for 6 min in SFC, necessary to establish the baseline of dissolution profiles. However, such an observation is not seen in RDE measurements as no hold is applied. This activity difference will be further elucidated and discussed later in the manuscript. However, when calculating the remaining OER activity at the end of the AST (Figure S2b), we still observe different degradation rates on GC and BDD relative to the LPL, while the degradation rate remains relatively constant for Au and IrO_2.

The GC and BDD backing electrodes exhibited a distinct and comparable relationship between the LPL and the OER activity (Figure 2a). The lowest activity was observed at an LPL of 0 V_{RHE}, while the highest activity occurred at LPLs of 1.23 V_{RHE} for GC and 1.4 V_{RHE} for BDD. Moreover, the OER activity increased linearly by increasing LPL values for both electrodes. In contrast, the activity on Au and IrO_2 electrodes showed no significant influence from the LPL, further confirming the inert nature of Au.[30,51] This evaluation of the OER performance of Ir black on different backing electrodes and LPLs sheds light on the intricate interplay among the catalyst, backing electrode, and the parameters of the AST.

To explain the observed activity trends, we estimated the average of integrated anodic and cathodic total charges of Ir from the CVs in the potential range of 0.4−1.4 V_{RHE} (Figure 2c), as further illustrated in Figure S3.[52] In the case of the IrO_2 backing electrode, the total average charge was corrected, as explained in detail in Section 3.3.4. Since the total average charge of Ir reflects its ECSA, for simplicity, we will refer to it as ECSA in this study. The analysis of the ECSA indicates that the Ir ECSA prior to AST is within a similar range, and the LPL applied during the AST has minimal influence on it for all backing electrodes except BDD. Further analysis reveals specific observations for each backing electrode. In the case of GC at 0 V_{RHE}, the Ir^{III}/Ir^{IV} peak is not observable on the CV. Therefore, it is excluded from the ECSA analysis and will be discussed in more detail below. For the Au backing electrode, the ECSA remains relatively constant from 1.1 to 1.4 V_{RHE}, but there is a slight increase observed at 0.9 and 0 V_{RHE}. On the other hand, the BDD electrode shows an increase in Ir ECSA at 1.1 V_{RHE} and 1.4 V_{RHE}, with no observable Ir^{III}/Ir^{IV} peak on the CV at 0 V_{RHE}, similar to GC. Finally, the IrO_2 backing electrode exhibits a consistent ECSA across all LPLs, similar to the Au electrode. Consequently, the decrease in the OER activity for GC and BDD seen in Figure 2a,b is likely due to factors other than discrepancies in catalyst loadings and potential effects of catalyst dissolution, which can increase the surface porosity and roughness.

To explain the trends observed in the OER activities, we conducted EIS measurements to determine the ohmic resistance of each catalyst spot in conjunction with the corresponding LPL,

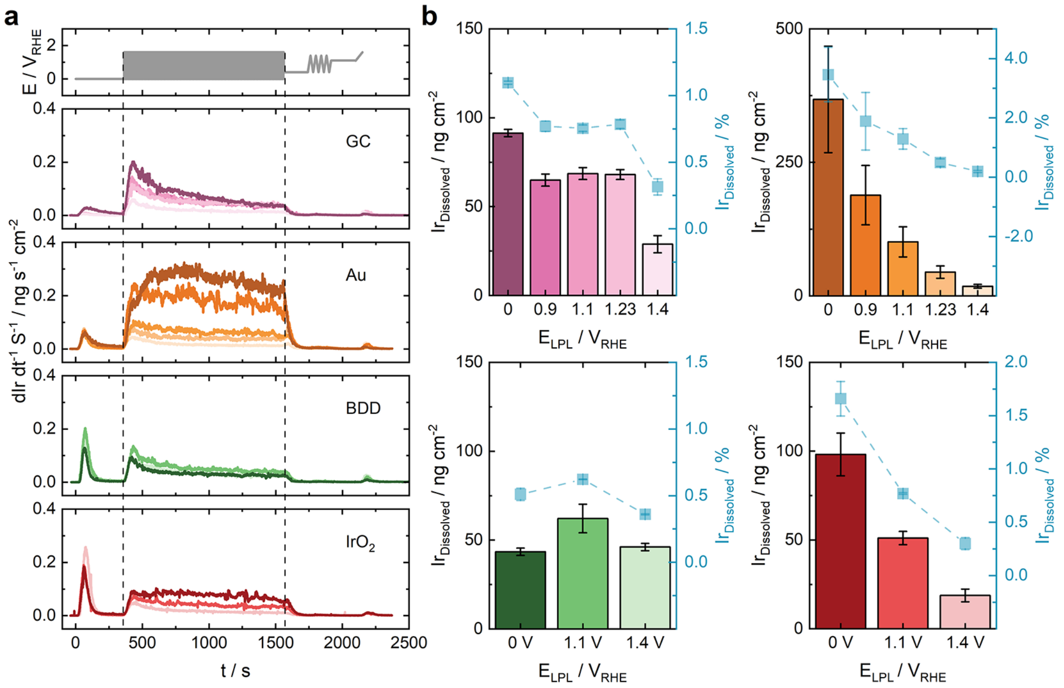

Figure 3. Impact of different LPLs in AST on the stability of Ir measured by SFC-ICP-MS. (a) Online ICP−MS dissolution profiles for Ir black on different backing electrodes (GC, Au, BDD, and IrO_2) during the applied electrochemical protocol, as depicted in Figure 1. (b) Quantification of the amount of Ir dissolved during the AST. The quantities are derived by integrating the corresponding dissolution profiles presented in (a). The left *Y*-axis (black) represents normalization by the surface area of the catalyst spot, while the right *Y*-axis (blue) represents normalization by the total amount of Ir in the sample. Backing electrode color coding: GC (purple), Au (orange), BDD (green), and IrO_2 (red); darker color tones represent lower LPL values.

as depicted in Figure S4. For GC, a pronounced increase in ohmic resistance is observed as the LPL increases, while it decreases at 0 V_{RHE} LPL. Notably, between 0 and 1.4 V_{RHE}, the resistance nearly doubles. In the case of Au and IrO_2 backing electrodes, however, the changes in resistances before and after AST are not as pronounced and are within the range of measurement tolerance. Conversely, an opposite trend is observed for the BDD electrode, with a substantial increase in resistance after the AST as the LPL decreases from 1.4 to 0 V_{RHE}. Correlating the activity trends shown in Figure 2a,b and the ohmic resistances, we can observe that a decrease in activity is accompanied by an increase and decrease in resistance for GC and an increase in resistance for BDD. In contrast, no significant changes in resistance are observed for Au and IrO_2, which aligns with the absence of significant changes in the OER activity.

Lastly, we analyzed the characteristic CV redox features of Ir black on all backing electrodes, as shown in Figure 2c. Notably, in the CV of GC, significant changes are observed following the AST with a LPL of 0 V_{RHE}. The anodic and cathodic peaks of the Ir^{III}/Ir^{IV} redox couple around 0.9 V_{RHE} are absent, while a new peak emerges around 0.55 V_{RHE}. The potential of this new peak aligns with previous studies on a well-known quinone/hydroquinone redox couple known to form at high potentials in acidic solutions.[32,53] To exclude the possibility that the observed effects were merely due to the delamination of the catalyst layer, we conducted a series of post-mortem SEM and energy dispersive X-ray spectroscopy (EDXS) measurements. Specifically, we compared the catalyst spot after the AST to that of the pristine Ir black. The results, as depicted in Figure S5a,b, demonstrate that the catalyst spot remains on the surface of the GC with a similar particle distribution. Further confirmation that the particles are indeed Ir was provided by SEM-EDXS analysis, as shown in Figure S5c,d, and the corresponding EDX spectra are presented in Figure S5e,f. Therefore, the changes observed in the CV in Figure 2c can be confidently attributed to factors other than delamination, such as the formation of a passivation layer on GC. We conducted XPS measurements to determine whether the GC passivation layer encapsulates the Ir particles or whether the layer forms between the Ir particles and the electrode surface (which could result in loss of contact). As seen in Figure S6a, before and after the AST, we observe two distinct peaks of Ir, consistent with previous reports.[54] Figure S6b shows increased binding energy for O 1s after the AST, suggesting further oxidation. However, the XPS results depicted in Figure S6 do not allow for a definitive conclusion regarding the encapsulation of Ir particles by the GC passivation layer. Two scenarios are plausible; either the GC passivation layer's thickness is beyond the sensitivity of XPS measurements or, more likely, the layer is situated between the Ir particles and the electrode surface, preventing electrical contact. Therefore, the current data leave the question unresolved, and further investigations are required to conclusively resolve this.

We hypothesize that in the case of GC, both low and high LPLs result in the formation of a passivated oxide layer on the electrode surface, influencing the observed changes in Ir activity and ohmic resistance. This further clarifies the absence of Ir^{III}/Ir^{IV} peaks on the CV measured after AST with an LPL of 0 V_{RHE}. Additionally, the increase in ohmic resistance with increasing LPL may also be attributed to the formation of a passivated layer during the AST, which arises from carbon oxidation at high anodic potentials.[31,32,34]

In the case of the Au backing electrode, after ASTs with different LPLs, we observe the emergence of new peaks in Figure 2c when the LPL is 1.23 V_{RHE} or lower, in addition to the $Ir^{III}/$

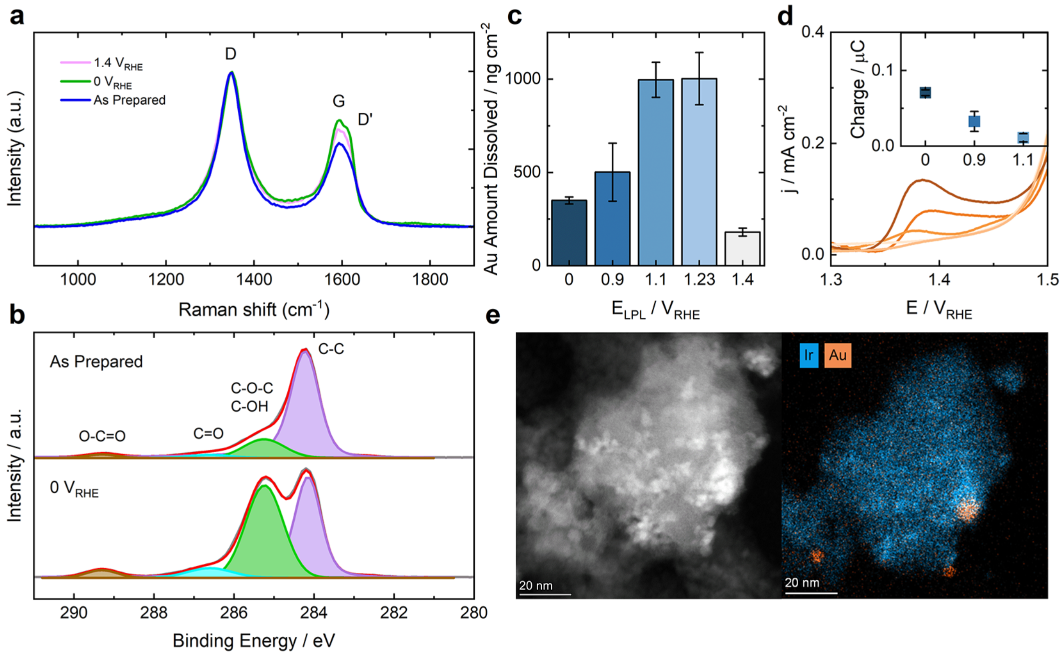

Figure 4. Degradation mechanisms of backing electrodes during the AST. (a) Raman spectra of the as-prepared GC, GC after the AST with 1.4 V_{RHE} LPL and 0 V_{RHE} LPL. For a more accurate comparison, the spectra are normalized based on the maximum intensity of the D band. (b) High-resolution XPS spectra of C 1s of the as-prepared BDD (top) and BDD after AST (bottom) with 0 V_{RHE} LPL (5000 pulses). (c) Quantification of Au dissolution during the AST with varied LPLs, obtained by integrating the corresponding dissolution profiles. (d) Magnified view of the Au-oxidation peak during the LSV from 1.3 to 1.5 V_{RHE} as shown in Figure 2a, following the AST with different LPLs. Inset: Anodic charge calculated by integration of the Au-oxidation peak. (e) HAADF-STEM (left) and STEM-EDXS (right) image of Ir black after 1000 pulses of AST with 0 V_{RHE} LPL measured by SFC.

Ir^{IV} peaks of Ir around 0.9 V_{RHE}. The anodic peak around 1.4 V_{RHE} corresponds to Au-oxidation, while the cathodic peak around 1.2 V_{RHE} is associated with the reduction of the formed Au oxide.[37] An additional anodic peak becomes evident at approximately 1.2 V_{RHE}. We hypothesize that this peak corresponds to the oxidation of single-atom Au species on the Ir surface. As a result of their high surface energy, the oxidation of these species could take place at lower potentials. These observations provide a possible explanation for the higher ECSA values of Ir seen in Figure S3.

Regarding the BDD electrode, it is noteworthy that the Ir^{III}/Ir^{IV} peaks around 0.9 V_{RHE} are absent after the AST with an LPL of 0 V_{RHE}. Instead, a new peak emerges at around 1.2−1.3 V_{RHE}. This newly observed peak becomes more pronounced with higher LPLs, which could potentially account for the observed increase in the total average charge in Figure S3. Combining these observations with the changes in conductivity and activity, we hypothesize that electrode degradation occurs similar to GC, hindering electron transfer at the Ir−BDD interface.

Finally, for the IrO_2 backing electrode, no changes are observed in the CVs presented in Figure 2c, which is consistent with the constant Ir ECSA values shown in Figure S3 and the activity trends displayed in Figure 2a,b. The slightly lower ECSA values compared to those of GC or Au may be attributed to the lower surface roughness of the IrO_2 thin film or its contribution to the ECSA estimation.

3.2. Exploring the Interplay between Ir Dissolution, Backing Electrode, and LPL.

In order to explain the changes in ECSA and activity, we analyze the dissolution stability of Ir as measured by online ICP−MS during the applied electrochemical protocol, as shown in Figure 3a,b.

In Figure 3a, we notice a marked increase in Ir dissolution at the beginning of the AST, resulting from a combination of two mechanisms of Ir dissolution. The first mechanism involves transient or passive dissolution resulting from the oxidation and reduction of metallic Ir.[39,55] This process includes anodic dissolution during oxide formation and cathodic dissolution during oxide reduction.[55] This mechanism becomes more pronounced as the LPL decreases. The second mechanism is transpassive dissolution, which results from the OER,[39] as the OER and Ir dissolution pathways share common intermediates.[56] Ir stabilizes after an initial surface reconstruction and is finally covered by a protective passive oxide layer, which results in lower OER-attributed dissolution.[4,55]

The integration of the area under the dissolution profiles in Figure 3a is shown in Figure 3b. The Ir dissolution is lowest at an LPL of 1.4 V_{RHE}, while the highest dissolution occurs at an LPL of 0 V_{RHE}, except for BDD. In the case of BDD, Ir dissolution at 0 V_{RHE} is comparable to that at 1.4 V_{RHE}. Previous studies by Cherevko et al.[55,57] demonstrated that cathodic Ir dissolution is significantly higher when the cathodic potential is lower, i.e., with a lower LPL value. Additionally, anodic dissolution rates are higher in anodic steps when more oxide is reduced during the preceding cathodic pulse. Therefore, the lowest dissolution at 1.4 V_{RHE} can be attributed to the absence of cathodic dissolution or oxide reduction as the LPL is too high.[39] Conversely, the highest dissolution at an LPL of 0 V_{RHE} can be attributed to the high overpotential required for the reduction of the formed oxide on the Ir surface,[40,58] as also proposed by Weiß et al. through scanning transmission electron microscopy (STEM) imaging in a PEMWE.[50] For GC, the consistent dissolution within the LPL range of 1.23 to 0.9 V_{RHE} can be explained by kinetic hindrances in oxide reduction at these potentials, which slow down the dissolution process.[55]

Comparatively, Ir dissolution on Au foil is significantly higher than that in GC, BDD, and IrO_2. We hypothesize it is caused by the extensive transient dissolution of Au from the backing electrode, resulting from oxidation and reduction occurring at lower LPLs, as discussed in more detail below.[36,37] This leads to surface roughening, which, in turn, further undermines the stability of Ir.[59]

The dissolution of Ir on BDD closely mirrors that observed on GC (Figure 3b). However, at an LPL of 0 V_{RHE}, the dissolution on BDD is nearly two times lower. This disparity may be attributed to a significant decrease in conductivity induced by the AST at this LPL, resulting in a high contact resistance and a higher *iR* drop. These factors should be considered when BDD is employed as a substrate in future measurements.

Lastly, the dissolution of Ir on IrO_2 backing electrodes, as determined through online ICP−MS measurements, demonstrates trends and values similar to those observed with GC. It is worth mentioning that the dissolution of the underlying IrO_2 substrate is subtracted from the dissolution of Ir black, as discussed in Section 3.3.4 of the manuscript. Notably, the stability of Ir black on IrO_2 remains unaffected by the extensive dissolution of the backing electrode or the high contact resistance, as observed with Au and BDD, respectively.

Based on the preceding discussion, it can be concluded that the observed OER activity losses in Figure 2a,b cannot be solely attributed to Ir dissolution on the different backing electrodes. Upon normalizing the dissolution data with the total loading of Ir on the electrodes (132.7 ng), Figure 3b, it is found that only approximately 0.5−1% to 0.3% of Ir is dissolved for 0 and 1.4 V_{RHE} LPL for GC, BDD, and IrO_2 backing electrodes. However, in the case of Au, the dissolved fraction ranges from ∼3.5 to 0.2% for 0 and 1.4 V_{RHE}, respectively.

3.3. Understanding the Degradation Processes of Backing Electrodes during the OER.

Given that the observed trends in Ir activity cannot be fully explained by dissolution alone, we hypothesize that the degradation of the backing electrode during AST could potentially contribute to the trends in Ir activity and stability, as previously reported.[31,34] Therefore, to investigate this possibility, we performed a series of surface characterization techniques on the GC, BDD, and Au backing electrodes before and after AST, as illustrated in Figure 4.

3.3.1. Passivation Mechanism of the GC Electrode during the OER.

Based on Ir CVs on GC in Figure 2c, GC passivation was identified as the primary mechanism responsible for the trend in Ir activity observed in Figure 2a,b. However, the relationship between GC passivation and the ohmic resistance observed in Figure S4 remains unclear. Prior studies have demonstrated that increasing the anodic potential during chronoamperometry leads to a higher concentration of oxygen functional groups on the GC surface.[33,53,60] As a result, one might expect that keeping the LPL higher during the AST would cause a higher degree of GC passivation, explaining the greater ohmic resistance of the GC backing electrode at higher LPLs (Figure S4). Nonetheless, this hypothesis contradicts the lower ohmic resistance seen at 0 V_{RHE}, observed changes in the CVs in Figure 2c and the higher Ir activity at 1.4 V_{RHE} compared to 0 V_{RHE} LPL (Figure 2a,b).

Various pretreatment techniques of GC have been thoroughly investigated in the literature.[60−63] Using XPS, multiple studies have shown that performing a reduction step after anodization can effectively remove oxygen from the oxide layer formed during the anodization process, thus restoring the conductivity of the nonconductive anodic layer at the GC.[60,61,63−65] This aligns with the ohmic resistance trend observed in this study (Figure S4). When the LPL is decreased to 0 V_{RHE}, there is a greater reduction of the anodic layer formed at 1.6 V_{RHE} on GC. This reduction results in the removal of oxygen from the layer, increasing its conductivity.

Considering all of the above, we can conclude that several mechanisms are involved in GC passivation, particularly when subjected to oxidizing and reducing potentials. According to previous reports, various pretreatment methods can alter the structure of the oxide film formed on the GC surface. Oxidation of GC leads to the formation of a dense oxide film, while the reduction of this film results in a three-dimensional oxide film that is more porous and partially conductive.[60−62,65] A further reduction of the anodically formed layer was reported to result in its electrochemical deactivation.[65] Using differential electrochemical mass spectrometry, Colmenares et al.[66] and later on, Ashton and Arenz[67] confirmed that complete passivation of the carbon surface at high potentials inhibits its further oxidation, and low potential excursions are necessary to reduce the surface and enable further oxidation. This was again corroborated by Pizzutilo et al.,[68] who tested Pt supported by carbon during AST protocols and reported that carbon corrosion increased by reducing the LPL, leading to lower Pt ECSA and a drop in its activity.

After considering all mentioned studies and combining them with our findings, we can propose a hypothesis regarding the observed activity trend for Ir, as shown in Figure 2a,b. Potentially, lowering the LPL leads to a thicker and partially conductive oxide layer structure on the GC, which can block the contact with Ir active sites and consequently results in lower activity. Conversely, a thinner and more compact oxide layer forms at more anodic LPL, which is less likely to prevent contact with the Ir sites at the time scale of the SFC protocol. We performed Raman spectroscopy on GC with drop-cast Ir following the SFC-ICP-MS measurement to validate our hypothesis. When no changes were initially detected, we hypothesized that the reason could be the low surface sensitivity of Raman spectroscopy, which might be insufficient to measure a formed passivation layer, assumed to be less than 100 nm thick. To overcome this issue and continue tracking changes in GC's passivation, we subjected GC, without Ir, to the same ASTs with 0 and 1.4 V_{RHE} LPL using 5000 pulses. This measurement aimed to create a thicker passivation film that could be detected by Raman spectroscopy.

The following Raman spectra of GC in Figure 4a can be correlated to the vibrational spectra of graphite.[69] It displays three prominent bands corresponding to resonant phonon vibrations of the graphitic structures at 1360, 1620, and 1580 cm^{-1}, denoted as D (defect), D′, and G (graphite) band, respectively. In Raman spectroscopy, both the G and D bands originate from sp^2 sites: while the G band indicates the presence of sp^2 networks, the D and D′ bands are associated with defects. Furthermore, the D band is linked to the breathing mode of sp^2 atoms in six-fold aromatic rings, while the G band occurs at all sp^2 sites, not just in rings, and is associated with the bond stretching of pairs of sp^2 atoms in both rings and chains. The intensity changes and the integrated intensity ratio of the D and G band (I_D/I_G) were used to estimate the degree of disorder and defect quantity in GC.[32,70−73]

Figure 4a shows a relative increase in the intensity of the local minimum at around 1500 cm^{-1} between the as-prepared sample and the sample measured after AST with both LPLs. It was previously suggested that this band originates from the amorphous sp^2-bonded forms of carbon, such as organic molecules, fragments, or functional groups.[32,73,74] This indicates that after the AST, carbon contains these oxidation-related species.[32] Furthermore, by lowering the LPL of the AST, the G band intensity increases, while the intensity ratio of D/G bands (I_D/I_G) decreases from ∼1.84 of the as-prepared sample to ∼1.45 after the AST with 0 V_{RHE} LPL.

According to the equation (eq 1) by Tuinstra and Koenig,[75] the relative peak intensity of the D and G bands is inversely proportional to the graphitic crystallite size in a sample.

$$\frac{I_D}{I_G} = \frac{C(\lambda)}{L_a} \tag{1}$$

Here, C is ∼4.4 nm for an excitation wavelength of 515.5 nm, and L_a represents the crystallite size. With decreasing LPL, the crystallite size of GC after the AST increases from 2.40 to 3.02 nm. However, it is important to note that eq 1 is only accurate for particles between 2.5 and 250 nm. Outside this range, corrections must be applied.[70] Therefore, the crystallite size values should be interpreted cautiously. Pimenta et al.[72] showed that electrical resistivity partly arises from carriers hopping between crystallites in samples. They observed that an increase in the crystallite size, as expected from lower LPLs, reduces resistivity, which is consistent with our findings (Figure S4). Additionally, lowering the LPL of the AST to 0 V_{RHE} causes a shoulder, known as the D′ peak, to appear on the G band. This peak emerges when significant disorder or an increase in the number of edge carbon atoms is present. It has been reported that in small crystals with limited three-dimensional order, the G and D′ peaks merge into a single, broader feature, as seen in the spectra of the as-prepared GC.[70,76]

The study of Yi et al.[32] observed an increase in the G band of GC after exposure to oxidative conditions in an acidic environment. Furthermore, the formation of functional groups was detected by infrared spectroscopy and XPS. Thus, we can conclude that the increase in the G band in our study, as the LPL of the AST decreases, leads to a higher degree of GC passivation.

Additionally, the XPS spectra of C 1s and O 1s were measured for the as-prepared GC, as well as GC samples treated with the AST using 0 and 1.4 V_{RHE} LPL, as shown in Figure S7a,b. These measurements aimed to identify functional groups present on the surface that may be responsible for the changes observed in the Raman spectra (Figure 4a). The intrinsic energy position of the C 1s main peak was adjusted to 284.5 eV to account for charging artifacts, as previously reported.[77] The analysis of the fitted C 1s spectra reveals the emergence of O−C═O bonds around 288.6 eV and C−O bonds around 285 eV following the AST. These findings are consistent with the previous literature,[33,34] further confirming that the surface of GC undergoes functionalization as a result of the AST. Additionally, by calculating the ratios of the integrated C−C to C═O and C−C to O−C═O peak areas, we observed a notable decrease in the C−C to C═O ratio on the surface after 0 V_{RHE} LPL compared to 1.4 V_{RHE} LPL (ratios of 10.7 and 6.75, respectively). Conversely, there was an increase in the level of the O−C═O species (with a C−C/O−C═O ratio of 8.7 to 9.5). However, it is crucial to interpret these values cautiously due to the potential presence of adventitious carbon residue on the sample's surface. Such residues could affect the measured C−C area and, subsequently, affect the calculated ratios. Furthermore, the O 1s peaks in Figure S7b show noticeable changes after the AST. Given the challenges associated with fitting the O 1s peak, we analyzed raw data.[33,78] According to a study by Yi et al.,[32] the appearance of a new shoulder at around 531.5 eV can be attributed to the formation of ═O bonds in carbonyls, lactones, anhydrides, or carboxyl groups following the AST with 0 V_{RHE} LPL. Another peak is observed around 533.4 eV, which can be correlated to −O bonds in hydroxyls, ethers, lactones, and carboxyl groups. The peak at 533.4 eV is also visible after AST with 1.4 V_{RHE} LPL, but to a lesser extent, as discussed earlier. These findings are consistent with the C 1s spectra, as shown in Figure S7a.

Lastly, it is important to note that both Raman and XPS measurements were performed on GC without drop-cast Ir, using the same protocol but with a longer AST. In the presence of Ir on the surface, higher currents and oxygen formation would occur due to the occurrence of OER, which would catalyze and accelerate the GC passivation, similar to what is observed during the ASTs with Ir and as previously reported for Pt.[79]

3.3.2. Passivation Mechanism of Boron-Doped Diamond Electrode during the OER. Previous studies have shown that BDD electrode kinetics is highly sensitive to surface termination, with surface conductivity decreasing when transitioning from H-terminated to O-terminated semiconducting diamond. Oxidation increases BDD films' surface resistance, impeding charge transfer at the diamond/solution interface. In contrast, hydrogenated diamond films have better conductivity than oxygenated ones.[80−82] Martin et al. suggested that hydrogen termination on the as-grown surface undergoes partial replacement by oxygen termination during polarization in an acidic solution. They showed an increase in the oxygen concentration (O/C ratio) after cathodic polarization, which was further increased when cycling between −2.0 and +3.0 V vs SHE (accompanied by significant H_2 and O_2 evolution).[83] Oxygen atoms are primarily incorporated onto the BDD surface through the reaction of carbon with $HO^\bullet$ radicals generated during the OER's initial step at high anodic potentials (eq 2) in acidic aqueous media.[84]

$$H_2O(BDD) \rightarrow HO^\bullet\,(BDD) + H^+ + e^- \tag{2}$$

They also demonstrated that surface O-termination can be achieved by applying highly positive current densities (tens of mA cm^{-2}) or potentials (approximately +2.0 V or less) for a few seconds to minutes.

Considering the Raman spectroscopy measurements of BDD in Figure S8a, the spectra reveal the sharp peak at 523 cm^{-1} and scattering in the range of 940−980 cm^{-1}, corresponding to Si phonon and Si second-order phonon, attributed to the Si wafer underneath the BDD film as a result of its transparency and thickness of 150 nm.[80] Upon closer analysis within the 1050 to 1800 cm^{-1} spectral range, distinct peaks emerge at 1220, 1320, and 1580 cm^{-1}. The peak around 1580 cm^{-1} was reported to correspond to crystalline graphite and increase in intensity at higher B content, suggesting that B doping results with increased graphitization at the grain boundaries.[85] Peaks at 1220 and 1320 cm^{-1} align with prior findings related to BDD.[80,85−87] Following the AST, a discernible reduction in the intensity of both peaks is evident. The decrease in intensity has been correlated with a lower concentration of boron in the BDD.[80,85,86]

To gain deeper insights into the surface chemistry, high-resolution XPS, a more surface-sensitive technique, was employed to investigate the surface properties of the as-prepared BDD and BDD films tested with 0 V_{RHE} LPL. The results are shown in Figures 4b and S9. Due to the charging effects, the intrinsic energy position of the C 1s main peak was aligned to 284.2 eV, as previously reported for BDD.[88] In the C

1s deconvoluted spectrum of the as-prepared BDD in Figure 4b, peaks at 284.2 eV correspond to sp^3 C−C present in the BDD bulk, while higher binding energy peaks at 285, 286.55, and 289 eV are associated with carbon in the form of C−OH or C−O−C, C═O, and COOH groups.[32−34,89,90] The small peak at around 282.6 eV can be assigned to sp^2 C═C, where reconstruction of the diamond surface, particularly at polycrystalline grain boundaries, may give rise to π bonding. After the AST, we observed a four-fold reduction in the ratios of C−C to C−O−C/C−OH integrated peak areas on the BDD surface compared to the as-prepared sample. Furthermore, the ratios of C−C to C═O and the ratio of O−C═O integrated peak areas also decreased by nearly half, indicating the functionalization and oxygen termination of the carbon on the BDD surface. This trend is consistent with our observations on the GC surface.

Furthermore, the O 1s spectrum of the as-prepared BDD in Figure S9a shows two distinct peaks at 532.4 and 533.8 eV, likely corresponding to oxygen bound to carbon, with the higher energy peak of the two possibly associated with −OH groups or adsorbed water molecules.[91] While we observe significant variations in the C 1s spectrum, the O 1s spectrum appears to remain unchanged before and after AST. To address this inconsistency, we hypothesized that the observed higher resistances and loss of conductivity in BDD at lower LPLs might be attributed to the potential loss of the boron dopant during the electrochemical tests, as indicated by Raman spectroscopy. To investigate this further, we conducted XPS measurements of the B 1s peak (Figure S9b) at around 186 eV. According to the findings of Yokoya et al.,[88] the peak corresponds to boron. Notably, this peak vanishes after the AST, while the same was not previously observed after a 25 h galvanostatic hold.[31] The peak at around 285.2 eV in Figure 4b can also be attributed to nondoped diamond, as reported in the same study by Yokoya et al.[88] Both of these observations align with the suggested hypothesis that boron is lost during AST. However, this finding contradicts the work of Denisenko et al.,[91] who attributed the 285.2 eV peak to C−O−C or C−OH. Nevertheless, we hypothesize that both effects could be at play, with the loss of boron during the AST and a potential functionalization of carbon on the surface. This implies that the peak around 285.2 eV may be a convolution of nondoped diamond and functionalized carbon on the surface. A more detailed study is necessary to validate these hypotheses.

In summary, the loss of the dopant or the surface functionalization could result in decreased conductivity, leading to a decrease in Ir ECSA and, ultimately, a decrease in the activity of Ir. To clarify, the apparent reduction in Ir ECSA does not mean that the active sites are lost. Instead, the Ir active sites are electrically isolated from the underlying substrate. This electrical disconnection leads to an observable loss of Ir ECSA as the catalytic sites become inactive due to their electric isolation.

3.3.3. Redeposition Mechanism of the Au Backing Electrode. To explain the Au-oxidation and reduction peaks in the CVs in Figure 2c, we must examine Au dissolution more closely during the AST. Figures S10 and 4c show that Au dissolution significantly decreases below 1.1 V_{RHE}. Combined with the CVs and the small oxidative current at around 1.4 V_{RHE} at the LSV in Figure 4d, we suggest that the kinetics of Au ion reduction near the working electrode increases significantly at these low potentials. Although the majority of the dissolved ions are expected to diffuse away from the electrode's vicinity, the rapid switching between high oxidative and reductive potentials under on/off pulsing can result in a considerable amount of Au ions redepositing back on the Au surface and Ir.[59,92] However, this is only possible at potentials lower than the onset of Au-oxidation, at around 1.25 V_{RHE}.[36] To validate these hypotheses, we conducted post-AST measurements on the sample after 1000 pulses with 0 V_{RHE} LPL using high-angle annular dark-field scanning transmission electron microscopy (HAADF-STEM) and STEM-EDXS, as illustrated in Figure 4e. The image reveals the presence of three smaller Au nanoparticles (orange) on agglomerated Ir nanoparticles (blue), indicating Au redeposition on the surface of Ir. Hence, the observed increase in Ir ECSA at 0 and 0.9 V_{RHE}, as depicted in Figure S3, can be attributed to the redeposition of Au onto Ir and its oxidation, thereby contributing to the total average charge. In reality, Au redeposition results in a reduction of Ir ECSA, as Au covers active sites, highlighting the inherent challenges in determining Ir ECSA with this method, especially when utilizing an Au backing electrode. A similar observation was reported by Jalalpoor et al., who investigated Pt supported by antimony-doped tin oxide. During the oxygen reduction reaction, they noted that the Sb dissolved from the support and redeposited on the Pt surface, lowering its ECSA.[93] Finally, in Figure 4c, the lower Au dissolution at the 1.4 V_{RHE} LPL is notably similar to the Ir dissolution shown in Figure 3. This similarity can be explained by the absence of cathodic dissolution, which is the dominant dissolution mechanism of Au below 1.6 V_{RHE}, as in the case of Ir.[36,59]

3.3.4. Understanding the Impact of the IrO_2 Backing Electrode on OER Activity/Stability of Ir Black. To accurately assess the activity and stability of the tested Ir-based electrocatalysts on the IrO_2 thin-film backing electrode, it is crucial to exclude the contribution of the latter on the OER activity as this backing electrode is intrinsically active for the OER. IrO_2 can add active sites but also undergoes dissolution, which can result in overestimating the catalyst's activity and underestimating its stability. This electrode contradicts the desired inert nature of backing electrodes, but it is possible to deconvolute its effects from the tested Ir catalyst.

Figure S11 presents the OER activity and stability of the IrO_2 thin film without drop-cast Ir black. When comparing its activity in Figure S11a,b with the activity of Ir black on the IrO_2 backing electrode (Figure 2a,b), we can observe that its activity is not significantly affected by the LPL of the AST and that the activity is ∼4 times lower than that of Ir black on IrO_2. However, this could pose a challenge for catalysts whose activity falls below that of IrO_2, and it is an important factor to keep in mind when utilizing the IrO_2 thin film as a backing electrode. Additionally, when comparing its dissolution in Figure S11d,e with the dissolution of Ir black on IrO_2 (Figure 3b), we find that its dissolution does not vary with different LPLs of AST, similar to its activity. Furthermore, the dissolution of IrO_2 is approximately ∼16, ∼8, and ∼4 times lower compared to the dissolution of Ir black during the AST at 0, 1.1, and 1.4 V_{RHE} LPL. This observation is consistent with previous reports highlighting the exceptional stability of IrO_2 during both anodic and cathodic polarizations.[40,41,94,95] This finding also implies that an even higher stability is anticipated when using more crystalline IrO_2.

We applied a correction method to improve the estimation of activity/stability of Ir black on IrO_2 backing electrodes in Figures 2, 3, and S3. We calculated the difference between the SFC surface area (0.033 cm^2) and the surface area of each measured Ir black catalyst spot. This difference was then multiplied by the corresponding values of activity, ECSA, and dissolution obtained for IrO_2. We subtracted these calculated

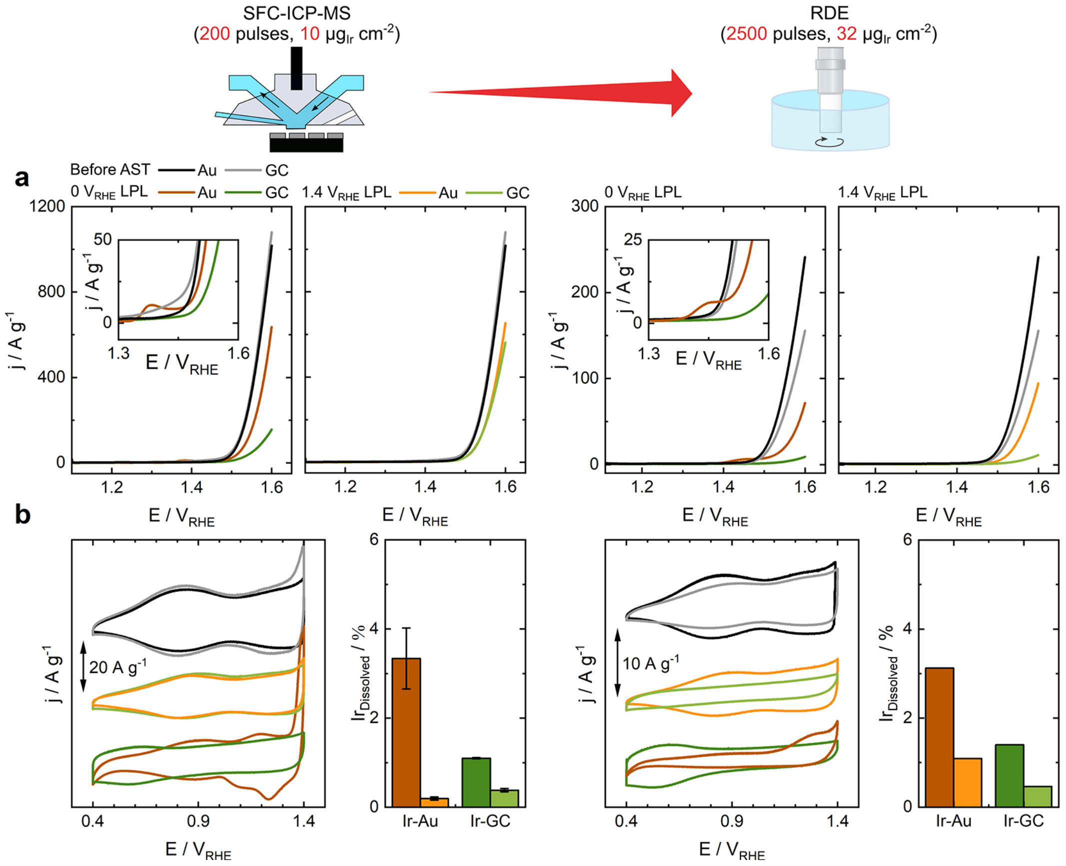

Figure 5. Comparing Ir activity and stability between the SFC-ICP-MS and RDE setup with extended AST and higher Ir loading. (a) LSV of Ir black on Au and GC, measured by SFC-ICP-MS (200 pulses) with 0 V$_{RHE}$ LPL and 1.4 V$_{RHE}$ LPL (left), and RDE (2500 pulses) on Au and GC tips at the same potentials (right). (b) CV of Ir black on Au and GC as measured by SFC-ICP-MS (left) and RDE (right), with corresponding Ir dissolution quantified by SFC-ICP-MS (left) and offline ICP-MS (right). CV was measured in the as-prepared state, after 1.4 V$_{RHE}$ LPL, and after 0 V$_{RHE}$ LPL AST. Offline ICP-MS analysis was performed on samples collected from the electrolyte following AST in the RDE setup. All dissolution amounts are normalized to the total Ir amount on the electrodes.

values from the corresponding values of the Ir black on IrO_2. This correction helped us obtain more precise measurements of the activity and stability of Ir black while excluding the contribution of the IrO_2 backing electrode.

3.4. Impact of Increased Loading and Extended ASTs: SFC-ICP-MS vs RDE.

To investigate whether the observed effects of the backing electrodes also occur with higher loading of Ir and longer ASTs, we increased the Ir loading three-fold and the number of pulses to 2500 instead of 200 in the RDE setup. We employed a H-cell with a porous frit, which should ensure a minimal Ir ion transfer into the counter electrode compartment and prevent their reduction and redeposition on the counter electrode. Due to the unavailability of commercial BDD and IrO_2 RDE tips, our investigation focused solely on GC and Au RDE tips. We selected the most extreme LPLs based on SFC-ICP-MS measurements of 0 and 1.4 V$_{RHE}$ to examine their impact on the mentioned backing electrodes.

Figure 5a displays the OER activities normalized by the mass of Ir black on Au and GC RDE tips compared with SFC-ICP-MS results.

The mass activities of Ir black in the SFC setup before AST align closely with previously reported values of ~1000 A g^{-1}.[96] Similarly, in the RDE configuration, the observed mass activities of ~250 A g^{-1} are consistent with findings reported by Alia and Anderson.[22] The discrepancy in the mass activity of Ir black between the SFC and RDE setups is evident, with Ir black demonstrating an approximately 4−5 times higher mass activity in the SFC. This difference can be attributed to the variation in the Nafion content in the ink used between the two setups. In SFC, the Nafion-to-catalyst ratio was 1:4, while in the RDE, it was 1:2.

This hypothesis aligns with earlier studies that reported reduced activity resulting from higher Ir loading and Nafion content.[22,26,35] At higher loadings, Ir utilization is lower due to thicker catalyst layers, while increased ionomer content leads to the contamination of Ir sites.[22] When normalized to Ir ECSA, the activity of SFC is also approximately 1.6 times higher (SFC: ~5.2 A C^{-1}, RDE: ~3.3 A C^{-1}), previously reported as a result of higher ionomer content.[22] More detailed results on this topic will be presented in our upcoming publication.

When comparing the activities before and after the AST, significantly higher degradation of Ir activity on both electrodes is evident in the RDE. The higher degradation is attributable to the 12.5 times more pulses during AST in the RDE. Considering the degradation mechanisms previously discussed in Sections 3.3.1−3.3.3 for each LPL, the longer protocol leads to a higher backing electrode and Ir degradation, resulting in increased loss of Ir active sites and a decrease in the OER activity.

Shifting our focus to the Ir activity at Au RDE tips, it is worth noting that at 0 V$_{RHE}$ LPL, the activity is slightly lower than that at 1.4 V$_{RHE}$. Figure S12 presents the Ir activities after 500 pulses during the AST to provide more detailed insights. The slightly higher activity after AST at 0 V_{RHE} can be explained by the initially higher activity at this potential compared to 1.4 V_{RHE} LPL. However, when considering degradation relative to the initial activity, it is evident that the degradation after AST at 0 V_{RHE} LPL is significantly higher, at 74%, compared to 55% at 1.4 V_{RHE} LPL. This discrepancy can be attributed to the observations in Section 3.3.3, where SFC-ICP-MS measurements showed increased Au dissolution followed by its redeposition at 0 V_{RHE} LPL, resulting in higher Ir dissolution as well. Notably, this was not observed at 1.4 V_{RHE} LPL. This difference in Ir activity degradation rates after AST between 0 and 1.4 V_{RHE} LPL can thus be attributed to these mechanisms. However, it is important to mention that the same differences were not observed in the SFC, potentially due to the shorter time scale of AST. This hypothesis is further supported by the appearance of the Au-oxidation peak around 1.45 V_{RHE}, as shown in Figure 5a inset, which aligns with the LSV of 0 V_{RHE} LPL from SFC-ICP-MS. Furthermore, the CV performed after AST with 0 V_{RHE} LPL (Figure 5b) exhibits a minor peak close to 1.3 V_{RHE}, indicating oxidation of single atomic Au. This is followed by a more pronounced oxidation peak of Au nanoparticles at 1.4 V_{RHE}, consistent with the SFC-ICP-MS findings for the 0 V_{RHE} LPL.

In contrast to the Au RDE tips, the GC electrodes displayed noticeably lower Ir activity following the AST for both LPLs. The SFC-ICP-MS results show that no GC passivation was observed at 1.4 V_{RHE}, compared to 0 V_{RHE}. A similar observation is seen in Figure S12 for the RDE, where after 500 pulses, the activity degradation is 68% for 0 V_{RHE} LPL and 42% for 1.4 V_{RHE} LPL. However, considering the significantly higher number of AST pulses applied in the RDE setup, the GC electrode becomes fully passivated after 2500 pulses, regardless of the LPL. This results in a complete decline in Ir activity. The CVs shown in Figures 5b and S12 provide supporting evidence, as there are no observable oxidation/reduction features of Ir seen after AST, while quinone/hydroquinone peaks emerge.

Lastly, in Figure 5b, we determined the dissolution of Ir by utilizing offline ICP−MS to analyze the electrolyte sample collected after the AST from the H-cell. Despite variations in loading and duration of the AST, a consistent trend in Ir dissolution is seen on both backing electrodes with both LPLs. At a higher LPL (1.4 V_{RHE}), the dissolution of Ir is notably lower compared to the lower LPL (0 V_{RHE}), aligning with the explanations provided earlier in the manuscript. Moreover, the dissolution of Ir on the Au electrode is significantly higher than that on the GC electrode.

Furthermore, between the RDE and SFC-ICP-MS setups, there is a good correlation between the dissolved amount of Ir normalized by its total loading. On the other hand, when comparing the dissolution of Ir normalized by the geometric surface area of the electrode (Figure S13), the dissolution on RDE is approximately three times higher than SFC, corresponding to the higher loading of Ir.

3.5. Impact of the Backing Electrode and LPL on Intrinsic OER Activity of Ir Black.

In the previous sections, we extensively examined the impact of the LPL and the backing electrode on the activity and stability of Ir black during the OER. Moreover, we provided an in-depth understanding of the degradation mechanisms of the backing electrodes. To ensure a more accurate assessment of Ir black's performance, we now focus on evaluating its intrinsic activity, which is normalized by the average of total anodic and cathodic charges. This allows us to highlight the intrinsic performance of the catalyst rather than rely solely on mass and geometric normalization influenced by the backing electrode. It is crucial to acknowledge that this method does have its limitations; it nevertheless provides valuable insights. The potential influence of charge contributions from the backing electrode on the precision of the Ir ECSA assessments is an important consideration. Combining this method in combination with EIS could provide a more distinct differentiation between double-layer and pseudocapacitive charge.[97] It is also important to reference the recent study by Lončar et al.,[98] which highlighted that the EIS method is not applicable for supported Ir-based nanopowders. Yet, given the potential insights provided by this method, its further exploration and potential applicability in future measurements are essential. However, despite the shortcomings of our ECSA determination by an average of total anodic and cathodic charge, we remain confident that the method is sufficient for our specific objectives, highlighting the influence of backing electrode degradation mechanisms without significantly influencing the ECSA estimation of Ir. In Figure 6, we present the intrinsic activity of Ir black measured at various LPLs during the AST on each of the investigated backing electrodes.

Regardless of the chosen backing electrode and the LPL applied during the AST, we observe a consistent and good correlation in the intrinsic activity of Ir black, with an

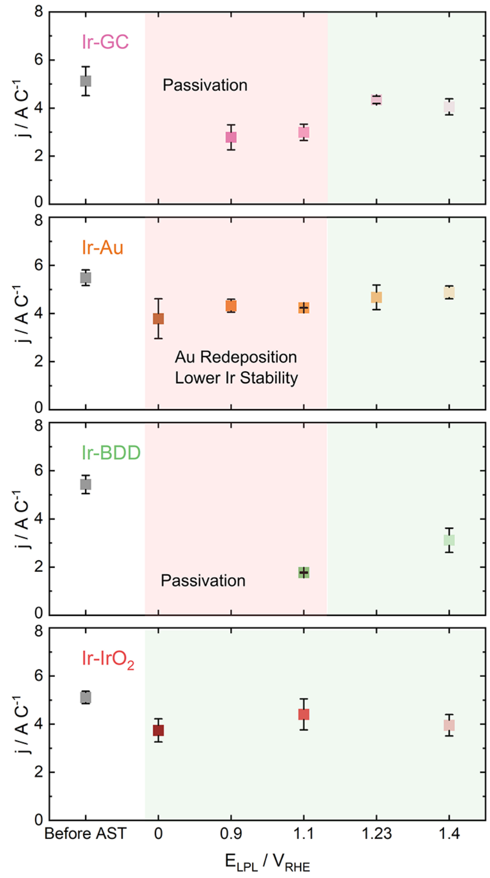

Figure 6. OER intrinsic activities of Ir black as measured by the SFC-ICP-MS setup on GC, Au, BDD, and IrO_2 backing electrodes following the AST with corresponding LPLs. The activities are normalized by the average of the total anodic and cathodic charge. The red area highlights the lower potential limits (LPLs) during AST that pose challenges in determining the intrinsic activity of iridium, while the green area represents optimal LPLs.

approximate value of 4 A C^{-1}, while the initial intrinsic activity of the as-prepared Ir black was ~5.5 A C^{-1}. The observed changes in its intrinsic activity following the AST can be attributed to the different degradation mechanisms of Ir taking place, such as loss of active sites by transient dissolution (depending on the LPL), OER-related dissolution, agglomeration, or alterations in the oxidation state during the OER.

By normalizing the OER activity of Ir based on its total average charge, we can mitigate the effects of electrode variations or catalyst layer quality. This normalization approach allows us to focus on the intrinsic performance of the catalyst, independent of the Ir mass or geometric surface area of the electrodes. However, it is important to note that this method is applicable only to Ir-based electrocatalysts, and there are certain LPLs of the AST where even this normalization approach is not effective (indicated by red areas in Figure 6) as it leads to significantly lower or undetermined intrinsic activity. This indicates that the degradation mechanisms of backing electrodes cannot be fully disregarded and ultimately affect the performance of the OER benchmarking.

We observed severe passivation on GC at 0 V_{RHE}, while some passivation was also observed at 1.4 V_{RHE}. However, the passivation at 1.4 V_{RHE} does not have any impact on the intrinsic activity of Ir within the time scale of the measurement in the SFC. Furthermore, by evaluating the intrinsic activity, we can observe that passivation of GC is evident at LPLs up to 1.23 V_{RHE}.

In the case of the Au backing electrode, we did not observe any changes in the intrinsic activity. However, the online ICP—MS data analysis suggested the possibility of redeposition of Au on Ir occurring below 1.1 V_{RHE}, which could result in the loss of active sites on Ir in longer ASTs. The STEM-EDXS measurements further supported this hypothesis. Additionally, the significant dissolution of Au also has an impact on the stability of Ir.

With the BDD backing electrodes, similar passivation patterns are observed, resembling the behavior on GC. The passivation is more severe at a lower LPL, specifically at 0 V_{RHE}.

Finally, when IrO_2 is used as the backing electrode, the intrinsic activity remains comparable across the different LPLs. However, it is important to note that IrO_2 does participate in the OER, although to a lesser extent. Therefore, as stated in Section 3.3.4, we corrected the intrinsic activity of Ir black by excluding the total average charge of IrO_2. Otherwise, it can lead to an underestimation of catalyst stability due to dissolution or an overestimation of activity as IrO_2 contributes to the overall OER.

4. CONCLUSIONS

In this study, we benchmarked and evaluated the activity and stability of a commercial Ir black catalyst on various backing electrodes during an AST with different LPLs using SFC-ICP-MS, Raman spectroscopy, XPS, SEM, and TEM. We demonstrated that both the LPL and the choice of backing electrode significantly impact the Ir activity and stability. We also revealed different degradation mechanisms occurring at the different LPLs for each backing electrode.

We observed two distinct passivation mechanisms for the GC electrode depending on the LPL during the AST. Higher and lower LPLs led to passivation, increasing the contact resistance between the catalyst and the electrode and decreasing the Ir ECSA. However, passivation was significantly more pronounced at lower LPLs.

In the case of the Au backing electrode, two undesirable effects hinder accurate Ir benchmarking. First, there is a significant increase in Au dissolution below 1.23 V_{RHE}, presumably resulting in the roughening of its surface and destabilization of Ir. This is evident from the considerably higher Ir dissolution than other backing electrodes. Additionally, with an LPL below 1.23 V_{RHE}, Au redeposition occurs on Ir, which further contributes to a decrease in the Ir ECSA, especially during longer ASTs.

The BDD electrode exhibited a behavior similar to that of GC, with lower LPLs leading to carbon surface functionalization, covering Ir active sites, and further reducing the conductivity of BDD, ultimately lowering Ir OER activity.

Finally, the IrO_2 thin-film backing electrode emerges as an excellent option due to its favorable characteristics, such as lack of passivation, good conductivity, resistance to reducibility under extreme cathodic potentials,[40] and good stability during anodic potentials.[41] Although it is not inert for the OER and can influence the catalyst's activity and dissolution, its impact can be predicted and properly accounted for. Moreover, its impact is minimal due to its low activity and high stability. Using IrO_2 as a backing electrode at higher temperatures and under reducing atmospheres presents a challenge due to the reduction of its surface layers to metallic Ir, which leads to decreased stability, although IrO_2 can hardly be reduced electrochemically.[99] As there are no commercially available IrO_2 RDE tips, an alternative approach would be to modify the RDE setup by incorporating thin-film electrode samples and drop-casting the desired catalyst onto the surface, as previously reported.[100]

Lastly, we recommend normalizing Ir-based catalyst activity by its ECSA, determined by integrating the total average charge from the CV.[101] This adjustment allows for a better comparison of catalyst activity across the literature. Even though 1.4 V_{RHE} LPL seems a better option, due to intense bubble formation, we propose using a 1.23 V_{RHE} LPL during the AST and an IrO_2 backing electrode as the testing conditions for benchmarking the OER catalysts.

By adhering to these guidelines, we can improve the estimation of catalyst lifetime and establish standardized test protocols to assess the performance of Ir-based electrocatalysts more accurately in AMSs. This will enable better correlation with the MEA performance, leading to the development of high-performing and more cost-effective catalysts. However, it is important to acknowledge and address the challenges that have received significant attention in AMSs, including issues related to bubbles, dissolution overestimation, and other relevant factors. Further investigation and solutions, such as gas diffusion electrodes, are still needed to mitigate these challenges effectively.

■ ASSOCIATED CONTENT

Supporting Information

The Supporting Information is available free of charge at https://pubs.acs.org/doi/10.1021/acscatal.3c03880.

> Detailed description of experimental protocols, SEM and laser profilometry images, XPS and Raman data, ICP—MS measurements data, and electrochemistry data (OER activity, ECSA, and Ohmic resistance) (PDF)

AUTHOR INFORMATION

Corresponding Authors

Matej Zlatar – *Forschungszentrum Jülich GmbH, Helmholtz-Institute Erlangen-Nürnberg for Renewable Energy (IEK-11), 91058 Erlangen, Germany; Department of Chemical and Biological Engineering, Friedrich-Alexander-Universität Erlangen-Nürnberg, 91058 Erlangen, Germany;* orcid.org/0000-0003-1041-5149; Email: m.zlatar@fz-juelich.de

Serhiy Cherevko – *Forschungszentrum Jülich GmbH, Helmholtz-Institute Erlangen-Nürnberg for Renewable Energy (IEK-11), 91058 Erlangen, Germany;* orcid.org/0000-0002-7188-4857; Email: s.cherevko@fz-juelich.de

Authors

Daniel Escalera-López – *Forschungszentrum Jülich GmbH, Helmholtz-Institute Erlangen-Nürnberg for Renewable Energy (IEK-11), 91058 Erlangen, Germany;* Present Address: Department of Interface Science, Fritz-Haber Institute of the Max-Planck Society, 14195 Berlin, Germany; orcid.org/0000-0002-2001-9775

Miquel Gamón Rodríguez – *Department of Surface and Plasma Science, Faculty of Mathematics and Physics, Charles University, 180 00 Praha 8, Czech Republic*

Tomáš Hrbek – *Department of Surface and Plasma Science, Faculty of Mathematics and Physics, Charles University, 180 00 Praha 8, Czech Republic*

Carina Götz – *Forschungszentrum Jülich GmbH, Helmholtz-Institute Erlangen-Nürnberg for Renewable Energy (IEK-11), 91058 Erlangen, Germany; Department of Chemical and Biological Engineering, Friedrich-Alexander-Universität Erlangen-Nürnberg, 91058 Erlangen, Germany*

Rani Mary Joy – *Institute for Materials Research (IMO), Hasselt University, 3590 Diepenbeek, Belgium; IMOMEC, IMEC vzw, 3590 Diepenbeek, Belgium*

Alan Savan – *Materials Discovery and Interfaces, Institute for Materials, Ruhr University Bochum, D-44801 Bochum, Germany*

Hoang Phi Tran – *Department of Chemistry, Chemical and Materials Engineering Division, the Electrochemical Energy, Catalysis and Materials Science Laboratory, Technische Universität Berlin, 10623 Berlin, Germany*

Hong Nhan Nong – *Department of Chemistry, Chemical and Materials Engineering Division, the Electrochemical Energy, Catalysis and Materials Science Laboratory, Technische Universität Berlin, 10623 Berlin, Germany;* orcid.org/0000-0002-3192-3479

Paulius Pobedinskas – *Institute for Materials Research (IMO), Hasselt University, 3590 Diepenbeek, Belgium; IMOMEC, IMEC vzw, 3590 Diepenbeek, Belgium;* orcid.org/0000-0001-8136-5172

Valentín Briega-Martos – *Forschungszentrum Jülich GmbH, Helmholtz-Institute Erlangen-Nürnberg for Renewable Energy (IEK-11), 91058 Erlangen, Germany;* orcid.org/0000-0001-8407-2260

Andreas Hutzler – *Forschungszentrum Jülich GmbH, Helmholtz-Institute Erlangen-Nürnberg for Renewable Energy (IEK-11), 91058 Erlangen, Germany;* orcid.org/0000-0001-5484-707X

Thomas Böhm – *Forschungszentrum Jülich GmbH, Helmholtz-Institute Erlangen-Nürnberg for Renewable Energy (IEK-11), 91058 Erlangen, Germany;* orcid.org/0000-0003-2036-2159

Ken Haenen – *Institute for Materials Research (IMO), Hasselt University, 3590 Diepenbeek, Belgium; IMOMEC, IMEC vzw, 3590 Diepenbeek, Belgium;* orcid.org/0000-0001-6711-7367

Alfred Ludwig – *Materials Discovery and Interfaces, Institute for Materials, Ruhr University Bochum, D-44801 Bochum, Germany*

Ivan Khalakhan – *Department of Surface and Plasma Science, Faculty of Mathematics and Physics, Charles University, 180 00 Praha 8, Czech Republic;* orcid.org/0000-0003-2929-4148

Peter Strasser – *Department of Chemistry, Chemical and Materials Engineering Division, the Electrochemical Energy, Catalysis and Materials Science Laboratory, Technische Universität Berlin, 10623 Berlin, Germany;* orcid.org/0000-0002-3884-436X

Complete contact information is available at: https://pubs.acs.org/10.1021/acscatal.3c03880

Author Contributions

M.Z. designed and performed SFC-ICP-MS, RDE measurements, and sample preparation for other characterizations (TEM, XPS, and Raman Spectroscopy), including evaluation and analysis of the data. M.G.R. and T.H. conducted XPS measurements. C.G. performed Raman Spectroscopy. A.H. conducted HAADF-STEM measurements. R.M.J. and P.P. prepared BDD samples. A.S. provided Ir thin films. D.E.-L., V.B.-M., H.P.T., H.N.N., A.L., I. K. and P. S. participated in discussions and provided valuable comments on the manuscript. M.Z. wrote the original draft. All authors reviewed and edited the manuscript and have given approval to the final version of the manuscript. D.E.-L. and S.C. supervised the experimental work.

Notes

The authors declare no competing financial interest.

ACKNOWLEDGMENTS

This work was supported by the Deutsche Forschungsgemeinschaft (DFG) within the grants CH 1763/4-1, STR 596/21-1, and STR596/11-1, including the Methusalem NANO network, and the Research Foundation—Flanders (FWO) via project G0D4920N. Lastly, M.G.R., T.H., and I.K. acknowledge the Czech Ministry of Education, Youth and Sports (Project LM2023072).

REFERENCES

(1) Buttler, A.; Spliethoff, H. Current status of water electrolysis for energy storage, grid balancing and sector coupling via power-to-gas and power-to-liquids: A review. *Renewable Sustainable Energy Rev.* **2018**, *82*, 2440–2454.

(2) European Climate Law. https://climate.ec.europa.eu/eu-action/european-green-deal/european-climate-law_en (accessed 31-07-2023).

(3) Shiva Kumar, S.; Himabindu, V. Hydrogen production by PEM water electrolysis - A review. *Mater. Sci. Energy Technol.* **2019**, *2* (3), 442–454.

(4) Cherevko, S.; Zeradjanin, A. R.; Topalov, A. A.; Kulyk, N.; Katsounaros, I.; Mayrhofer, K. J. J. Dissolution of Noble Metals during Oxygen Evolution in Acidic Media. *ChemCatChem* **2014**, *6* (8), 2219–2223.

(5) Minke, C.; Suermann, M.; Bensmann, B.; Hanke-Rauschenbach, R. Is iridium demand a potential bottleneck in the realization of large-scale PEM water electrolysis? *Int. J. Hydrogen Energy* **2021**, *46* (46), 23581–23590.

(6) Hubert, M. A.; King, L. A.; Jaramillo, T. F. Evaluating the Case for Reduced Precious Metal Catalysts in Proton Exchange Membrane Electrolyzers. *ACS Energy Lett.* **2022**, *7* (1), 17−23.

(7) Clapp, M.; Zalitis, C. M.; Ryan, M. Perspectives on current and future iridium demand and iridium oxide catalysts for PEM water electrolysis. *Catal. Today* **2023**, *420*, 114140.

(8) DOE Technical Targets for Hydrogen Production from Electrolysis. https://www.energy.gov/eere/fuelcells/doe-technical-targets-hydrogen-production-electrolysis (accessed 16-02-2022).

(9) Hydrogen Shot - Hydrogen and Fuel Cell Technologies Office. https://www.energy.gov/eere/fuelcells/hydrogen-shot (accessed 16-02-2022).

(10) Babic, U.; Suermann, M.; Büchi, F. N.; Gubler, L.; Schmidt, T. J. Critical Review—Identifying Critical Gaps for Polymer Electrolyte Water Electrolysis Development. *J. Electrochem. Soc.* **2017**, *164* (4), F387−F399.

(11) Ehelebe, K.; Escalera-López, D.; Cherevko, S. Limitations of aqueous model systems in the stability assessment of electrocatalysts for oxygen reactions in fuel cell and electrolyzers. *Curr. Opin. Electrochem.* **2021**, *29*, 100832.

(12) Lazaridis, T.; Stühmeier, B. M.; Gasteiger, H. A.; El-Sayed, H. A. Capabilities and limitations of rotating disk electrodes versus membrane electrode assemblies in the investigation of electrocatalysts. *Nat. Catal.* **2022**, *5* (5), 363−373.

(13) Geiger, S.; Kasian, O.; Ledendecker, M.; Pizzutilo, E.; Mingers, A. M.; Fu, W. T.; Diaz-Morales, O.; Li, Z.; Oellers, T.; Fruchter, L.; Ludwig, A.; Mayrhofer, K. J. J.; Koper, M. T. M.; Cherevko, S. The stability number as a metric for electrocatalyst stability benchmarking. *Nat. Catal.* **2018**, *1* (7), 508−515.

(14) Knöppel, J.; Möckl, M.; Escalera-López, D.; Stojanovski, K.; Bierling, M.; Böhm, T.; Thiele, S.; Rzepka, M.; Cherevko, S. On the limitations in assessing stability of oxygen evolution catalysts using aqueous model electrochemical cells. *Nat. Commun.* **2021**, *12* (1), 2231.

(15) McCrory, C. C. L.; Jung, S.; Peters, J. C.; Jaramillo, T. F. Benchmarking Heterogeneous Electrocatalysts for the Oxygen Evolution Reaction. *J. Am. Chem. Soc.* **2013**, *135* (45), 16977−16987.

(16) McCrory, C. C. L.; Jung, S.; Ferrer, I. M.; Chatman, S. M.; Peters, J. C.; Jaramillo, T. F. Benchmarking Hydrogen Evolving Reaction and Oxygen Evolving Reaction Electrocatalysts for Solar Water Splitting Devices. *J. Am. Chem. Soc.* **2015**, *137* (13), 4347−4357.

(17) Spöri, C.; Kwan, J. T. H.; Bonakdarpour, A.; Wilkinson, D. P.; Strasser, P. The Stability Challenges of Oxygen Evolving Catalysts: Towards a Common Fundamental Understanding and Mitigation of Catalyst Degradation. *Angew. Chem., Int. Ed.* **2017**, *56* (22), 5994−6021.

(18) Kuhnert, E.; Hacker, V.; Bodner, M. A Review of Accelerated Stress Tests for Enhancing MEA Durability in PEM Water Electrolysis Cells. *Int. J. Energy Res.* **2023**, *2023*, 3183108.

(19) Rakousky, C.; Reimer, U.; Wippermann, K.; Kuhri, S.; Carmo, M.; Lueke, W.; Stolten, D. Polymer electrolyte membrane water electrolysis: Restraining degradation in the presence of fluctuating power. *J. Power Sources* **2017**, *342*, 38−47.

(20) Alia, S. M.; Pylypenko, S.; Neyerlin, K. C.; Kocha, S. S.; Pivovar, B. S. Activity and Durability of Iridium Nanoparticles in the Oxygen Evolution Reaction. *ECS Trans.* **2015**, *69* (17), 883−892.

(21) Spöri, C.; Brand, C.; Kroschel, M.; Strasser, P. Accelerated Degradation Protocols for Iridium-Based Oxygen Evolving Catalysts in Water Splitting Devices. *J. Electrochem. Soc.* **2021**, *168* (3), 034508.

(22) Alia, S. M.; Anderson, G. C. Iridium Oxygen Evolution Activity and Durability Baselines in Rotating Disk Electrode Half-Cells. *J. Electrochem. Soc.* **2019**, *166* (4), F282−F294.

(23) Voronova, A.; Kim, H.-J.; Jang, J. H.; Park, H.-Y.; Seo, B. Effect of low voltage limit on degradation mechanism during high-frequency dynamic load in proton exchange membrane water electrolysis. *Int. J. Energy Res.* **2022**, *46* (9), 11867−11878.

(24) El-Sayed, H. A.; Weiß, A.; Olbrich, L. F.; Putro, G. P.; Gasteiger, H. A. OER Catalyst Stability Investigation Using RDE Technique: A Stability Measure or an Artifact? *J. Electrochem. Soc.* **2019**, *166* (8), F458−F464.

(25) Trogisch, N.; Koch, M.; El Sawy, E. N.; El-Sayed, H. A. Microscopic Bubble Accumulation: The Missing Factor in Evaluating Oxygen Evolution Catalyst Stability during Accelerated Stress Tests. *ACS Catal.* **2022**, *12* (21), 13715−13724.

(26) Fathi Tovini, M.; Hartig-Weiß, A.; Gasteiger, H. A.; El-Sayed, H. A. The Discrepancy in Oxygen Evolution Reaction Catalyst Lifetime Explained: RDE vs MEA - Dynamicity within the Catalyst Layer Matters. *J. Electrochem. Soc.* **2021**, *168* (1), 014512.

(27) Hartig-Weiss, A.; Tovini, M. F.; Gasteiger, H. A.; El-Sayed, H. A. OER Catalyst Durability Tests Using the Rotating Disk Electrode Technique: The Reason Why This Leads to Erroneous Conclusions. *ACS Appl. Energy Mater.* **2020**, *3* (11), 10323−10327.

(28) Petzoldt, P. J.; Kwan, J. T. H.; Bonakdarpour, A.; Wilkinson, D. P. Deconvoluting Reversible and Irreversible Degradation Phenomena in OER Catalyst Coated Membranes Using a Modified RDE Technique. *J. Electrochem. Soc.* **2021**, *168* (2), 026507.

(29) Koderman Podboršek, G.; Kamšek, A. R.; Lončar, A.; Bele, M.; Suhadolnik, L.; Jovanovič, P.; Hodnik, N. Atomically-resolved structural changes of ceramic supported nanoparticulate oxygen evolution reaction Ir catalyst. *Electrochim. Acta* **2022**, *426*, 140800.

(30) Benck, J. D.; Pinaud, B. A.; Gorlin, Y.; Jaramillo, T. F. Substrate Selection for Fundamental Studies of Electrocatalysts and Photoelectrodes: Inert Potential Windows in Acidic, Neutral, and Basic Electrolyte. *PLoS One* **2014**, *9* (10), No. e107942.

(31) Geiger, S.; Kasian, O.; Mingers, A. M.; Nicley, S. S.; Haenen, K.; Mayrhofer, K. J. J.; Cherevko, S. Catalyst Stability Benchmarking for the Oxygen Evolution Reaction: The Importance of Backing Electrode Material and Dissolution in Accelerated Aging Studies. *ChemSusChem* **2017**, *10* (21), 4140−4143.

(32) Yi, Y.; Weinberg, G.; Prenzel, M.; Greiner, M.; Heumann, S.; Becker, S.; Schlögl, R. Electrochemical corrosion of a glassy carbon electrode. *Catal. Today* **2017**, *295*, 32−40.

(33) Choudhury, S. H.; Ding, Y.; Yi, Y.; Rohner, C.; Frandsen, W.; Lunkenbein, T.; Greiner, M.; Schlögl, R.; Heumann, S. Oxidation Behavior of Glassy Carbon in Acidic Electrolyte. *ChemElectroChem* **2022**, *9* (20), No. e202200637.

(34) Edgington, J.; Deberghes, A.; Seitz, L. C. Glassy Carbon Substrate Oxidation Effects on Electrode Stability for Oxygen Evolution Reaction Catalysis Stability Benchmarking. *ACS Appl. Energy Mater.* **2022**, *5* (10), 12206−12218.

(35) Alia, S. M.; Rasimick, B.; Ngo, C.; Neyerlin, K. C.; Kocha, S. S.; Pylypenko, S.; Xu, H.; Pivovar, B. S. Activity and Durability of Iridium Nanoparticles in the Oxygen Evolution Reaction. *J. Electrochem. Soc.* **2016**, *163* (11), F3105−F3112.

(36) Cherevko, S.; Topalov, A. A.; Katsounaros, I.; Mayrhofer, K. J. J. Electrochemical dissolution of gold in acidic medium. *Electrochem. Commun.* **2013**, *28*, 44−46.

(37) Cherevko, S.; Zeradjanin, A. R.; Keeley, G. P.; Mayrhofer, K. J. J. A Comparative Study on Gold and Platinum Dissolution in Acidic and Alkaline Media. *J. Electrochem. Soc.* **2014**, *161* (12), H822−H830.

(38) Loncar, A.; Moriau, L.; Stojanovski, K.; Ruiz-Zepeda, F.; Jovanovic, P.; Bele, M.; Gaberscek, M.; Hodnik, N. Ir/TiONx/C high-performance oxygen evolution reaction nanocomposite electrocatalysts in acidic media: synthesis, characterization and electrochemical benchmarking protocol. *J. Phys.: Energy* **2020**, *2* (2), 02LT01.

(39) Cherevko, S. Electrochemical Dissolution of Noble Metals. In *Encyclopedia of Interfacial Chemistry*; Wandelt, K., Ed.; Elsevier, 2018, pp 68−75.

(40) Weber, T.; Vonk, V.; Abb, M. J. S.; Evertsson, J.; Sandroni, M.; Drnec, J.; Stierle, A.; Lundgren, E.; Over, H. Extraordinary Stability of IrO2(110) Ultrathin Films Supported on TiO2(110) under Cathodic Polarization. *J. Phys. Chem. Lett.* **2020**, *11* (21), 9057−9062.

(41) Weber, T.; Vonk, V.; Escalera-López, D.; Abbondanza, G.; Larsson, A.; Koller, V.; Abb, M. J. S.; Hegedüs, Z.; Bäcker, T.; Lienert, U.; Harlow, G. S.; Stierle, A.; Cherevko, S.; Lundgren, E.; Over, H. Operando Stability Studies of Ultrathin Single-Crystalline IrO2(110)

Films under Acidic Oxygen Evolution Reaction Conditions. *ACS Catal.* **2021**, *11* (20), 12651−12660.

(42) Zlatar, M.; Nater, D.; Escalera-López, D.; Joy, R. M.; Pobedinskas, P.; Haenen, K.; Copéret, C.; Cherevko, S. Evaluating the stability of Ir single atom and Ru atomic cluster oxygen evolution reaction electrocatalysts. *Electrochim. Acta* **2023**, *444*, 141982.

(43) Klemm, S. O.; Topalov, A. A.; Laska, C. A.; Mayrhofer, K. J. J. Coupling of a high throughput microelectrochemical cell with online multielemental trace analysis by ICP-MS. *Electrochem. Commun.* **2011**, *13* (12), 1533−1535.

(44) Klemm, S. O.; Karschin, A.; Schuppert, A. K.; Topalov, A. A.; Mingers, A. M.; Katsounaros, I.; Mayrhofer, K. J. J. Time and potential resolved dissolution analysis of rhodium using a microelectrochemical flow cell coupled to an ICP-MS. *J. Electroanal. Chem.* **2012**, *677−680*, 50−55.

(45) Oh, H.-S.; Nong, H. N.; Reier, T.; Gliech, M.; Strasser, P. Oxide-supported Ir nanodendrites with high activity and durability for the oxygen evolution reaction in acid PEM water electrolyzers. *Chem. Sci.* **2015**, *6* (6), 3321−3328.

(46) Tan, X.; Shen, J.; Semagina, N.; Secanell, M. Decoupling structure-sensitive deactivation mechanisms of Ir/IrOx electrocatalysts toward oxygen evolution reaction. *J. Catal.* **2019**, *371*, 57−70.

(47) Inaba, M.; Quinson, J.; Arenz, M. pH matters: The influence of the catalyst ink on the oxygen reduction activity determined in thin film rotating disk electrode measurements. *J. Power Sources* **2017**, *353*, 19−27.

(48) Papakonstantinou, G.; Algara-Siller, G.; Teschner, D.; Vidaković-Koch, T.; Schlögl, R.; Sundmacher, K. Degradation study of a proton exchange membrane water electrolyzer under dynamic operation conditions. *Appl. Energy* **2020**, *280*, 115911.

(49) Milosevic, M.; Böhm, T.; Körner, A.; Bierling, M.; Winkelmann, L.; Ehelebe, K.; Hutzler, A.; Suermann, M.; Thiele, S.; Cherevko, S. In Search of Lost Iridium: Quantification of Anode Catalyst Layer Dissolution in Proton Exchange Membrane Water Electrolyzers. *ACS Energy Lett.* **2023**, *8* (6), 2682−2688.

(50) Weiß, A.; Siebel, A.; Bernt, M.; Shen, T. H.; Tileli, V.; Gasteiger, H. A. Impact of Intermittent Operation on Lifetime and Performance of a PEM Water Electrolyzer. *J. Electrochem. Soc.* **2019**, *166* (8), F487−F497.

(51) Hammer, B.; Norskov, J. K. Why gold is the noblest of all the metals. *Nature* **1995**, *376* (6537), 238−240.

(52) Reier, T.; Pawolek, Z.; Cherevko, S.; Bruns, M.; Jones, T.; Teschner, D.; Selve, S.; Bergmann, A.; Nong, H. N.; Schlögl, R.; Mayrhofer, K. J. J.; Strasser, P. Molecular Insight in Structure and Activity of Highly Efficient, Low-Ir Ir-Ni Oxide Catalysts for Electrochemical Water Splitting (OER). *J. Am. Chem. Soc.* **2015**, *137* (40), 13031−13040.

(53) Dekanski, A.; Stevanović, J.; Stevanović, R.; Nikolić, B. Ž.; Jovanović, V. M. Glassy carbon electrodes: I. Characterization and electrochemical activation. *Carbon* **2001**, *39* (8), 1195−1205.

(54) Pfeifer, V.; Jones, T. E.; Velasco Vélez, J. J.; Massué, C.; Arrigo, R.; Teschner, D.; Girgsdies, F.; Scherzer, M.; Greiner, M. T.; Allan, J.; Hashagen, M.; Weinberg, G.; Piccinin, S.; Hävecker, M.; Knop-Gericke, A.; Schlögl, R. The electronic structure of iridium and its oxides. *Surf. Interface Anal.* **2016**, *48* (5), 261−273.

(55) Cherevko, S.; Geiger, S.; Kasian, O.; Mingers, A.; Mayrhofer, K. J. J. Oxygen evolution activity and stability of iridium in acidic media. Part 1. - Metallic iridium. *J. Electroanal. Chem.* **2016**, *773*, 69−78.

(56) Kasian, O.; Grote, J.-P.; Geiger, S.; Cherevko, S.; Mayrhofer, K. J. J. The Common Intermediates of Oxygen Evolution and Dissolution Reactions during Water Electrolysis on Iridium. *Angew. Chem., Int. Ed.* **2018**, *57* (9), 2488−2491.

(57) Cherevko, S.; Geiger, S.; Kasian, O.; Mingers, A.; Mayrhofer, K. J. J. Oxygen evolution activity and stability of iridium in acidic media. Part 2. - Electrochemically grown hydrous iridium oxide. *J. Electroanal. Chem.* **2016**, *774*, 102−110.

(58) Cherevko, S.; Geiger, S.; Kasian, O.; Kulyk, N.; Grote, J.-P.; Savan, A.; Shrestha, B. R.; Merzlikin, S.; Breitbach, B.; Ludwig, A.; Mayrhofer, K. J. J. Oxygen and hydrogen evolution reactions on Ru, RuO2, Ir, and IrO2 thin film electrodes in acidic and alkaline electrolytes: A comparative study on activity and stability. *Catal. Today* **2016**, *262*, 170−180.

(59) Cherevko, S.; Topalov, A. A.; Zeradjanin, A. R.; Katsounaros, I.; Mayrhofer, K. J. J. Gold dissolution: towards understanding of noble metal corrosion. *RSC Adv.* **2013**, *3* (37), 16516−16527.

(60) Sullivan, M. G.; Schnyder, B.; Bärtsch, M.; Alliata, D.; Barbero, C.; Imhof, R.; Kötz, R. Electrochemically Modified Glassy Carbon for Capacitor Electrodes Characterization of Thick Anodic Layers by Cyclic Voltammetry, Differential Electrochemical Mass Spectrometry, Spectroscopic Ellipsometry, X-Ray Photoelectron Spectroscopy, FTIR, and AFM. *J. Electrochem. Soc.* **2000**, *147* (7), 2636.

(61) Zhao, Q.-L.; Zhang, Z.-L.; Bao, L.; Pang, D.-W. Surface structure-related electrochemical behaviors of glassy carbon electrodes. *Electrochem. Commun.* **2008**, *10* (2), 181−185.

(62) Barbero, C.; Kötz, R. Electrochemical Activation of Glassy Carbon: Spectroscopic Ellipsometry of Surface Phase Formation. *J. Electrochem. Soc.* **1993**, *140* (1), 1−6.

(63) Cabaniss, G. E.; Diamantis, A. A.; Murphy, W. R., Jr.; Linton, R. W.; Meyer, T. J. Electrocatalysis of proton-coupled electron-transfer reactions at glassy carbon electrodes. *J. Am. Chem. Soc.* **1985**, *107* (7), 1845−1853.

(64) Wang, J.; Martinez, T.; Yaniv, D. R.; McConnick, L. D. In situ characterization of electrochemically activated glassy carbon electrodes with scanning tunneling microscopy. *J. Electroanal. Chem. Interfacial Electrochem.* **1990**, *278* (1−2), 379−386.

(65) Kepley, L. J.; Bard, A. J. Ellipsometric, electrochemical, and elemental characterization of the surface phase produced on glassy carbon electrodes by electrochemical activation. *Anal. Chem.* **1988**, *60* (14), 1459−1467.

(66) Colmenares, L. C.; Wurth, A.; Jusys, Z.; Behm, R. J. Model study on the stability of carbon support materials under polymer electrolyte fuel cell cathode operation conditions. *J. Power Sources* **2009**, *190* (1), 14−24.

(67) Ashton, S. J.; Arenz, M. A DEMS study on the electrochemical oxidation of a high surface area carbon black. *Electrochem. Commun.* **2011**, *13* (12), 1473−1475.

(68) Pizzutilo, E.; Geiger, S.; Grote, J. P.; Mingers, A.; Mayrhofer, K. J. J.; Arenz, M.; Cherevko, S. On the Need of Improved Accelerated Degradation Protocols (ADPs): Examination of Platinum Dissolution and Carbon Corrosion in Half-Cell Tests. *J. Electrochem. Soc.* **2016**, *163* (14), F1510−F1514.

(69) Soukup, L.; Gregora, I.; Jastrabik, L.; Koňáková, A. Raman spectra and electrical conductivity of glassy carbon. *Mater. Sci. Eng. B* **1992**, *11* (1−4), 355−357.

(70) Ferrari, A. C.; Robertson, J. Interpretation of Raman spectra of disordered and amorphous carbon. *Phys. Rev. B* **2000**, *61* (20), 14095−14107.

(71) Ferrari, A. C.; Robertson, J.; Ferrari, A. C.; Robertson, J. Raman spectroscopy of amorphous, nanostructured, diamond-like carbon, and nanodiamond. *Philos. Trans. R. Soc. London, Ser. A* **2004**, *362* (1824), 2477−2512.

(72) Pimenta, M. A.; Dresselhaus, G.; Dresselhaus, M. S.; Cançado, L. G.; Jorio, A.; Saito, R. Studying disorder in graphite-based systems by Raman spectroscopy. *Phys. Chem. Chem. Phys.* **2007**, *9* (11), 1276−1290.

(73) Sadezky, A.; Muckenhuber, H.; Grothe, H.; Niessner, R.; Pöschl, U. Raman microspectroscopy of soot and related carbonaceous materials: Spectral analysis and structural information. *Carbon* **2005**, *43* (8), 1731−1742.

(74) Jawhari, T.; Roid, A.; Casado, J. Raman spectroscopic characterization of some commercially available carbon black materials. *Carbon* **1995**, *33* (11), 1561−1565.

(75) Tuinstra, F.; Koenig, J. L. Raman Spectrum of Graphite. *J. Chem. Phys.* **1970**, *53* (3), 1126−1130.

(76) Escribano, R.; Sloan, J. J.; Siddique, N.; Sze, N.; Dudev, T. Raman spectroscopy of carbon-containing particles. *Vib. Spectrosc.* **2001**, *26* (2), 179−186.

(77) Chen, X.; Wang, X.; Fang, D. A review on C1s XPS-spectra for some kinds of carbon materials. *Fullerenes, Nanotubes Carbon Nanostruct.* **2020**, *28* (12), 1048−1058.

(78) Li, H. Determination of Oxygen Functionality on Highly Oriented Pyrolytic Graphite (HOPG). Ph.D. Thesis, Freie Universität Berlin, FU, Berlin, 2012.

(79) Lafforgue, C.; Chatenet, M.; Dubau, L.; Dekel, D. R. Accelerated Stress Test of Pt/C Nanoparticles in an Interface with an Anion-Exchange Membrane—An Identical-Location Transmission Electron Microscopy Study. *ACS Catal.* **2018**, *8* (2), 1278−1286.

(80) Schwarzová-Pecková, K.; Vosáhlová, J.; Barek, J.; Šloufová, I.; Pavlova, E.; Petrák, V.; Zavázalová, J. Influence of boron content on the morphological, spectral, and electroanalytical characteristics of anodically oxidized boron-doped diamond electrodes. *Electrochim. Acta* **2017**, *243*, 170−182.

(81) Yagi, I.; Notsu, H.; Kondo, T.; Tryk, D. A.; Fujishima, A. Electrochemical selectivity for redox systems at oxygen-terminated diamond electrodes. *J. Electroanal. Chem.* **1999**, *473* (1−2), 173−178.

(82) Liu, F. B.; Wang, J. D.; Liu, B.; Li, X. M.; Chen, D. R. Effect of electronic structures on electrochemical behaviors of surface-terminated boron-doped diamond film electrodes. *Diamond Relat. Mater.* **2007**, *16* (3), 454−460.

(83) Martin, H. B.; Argoitia, A.; Angus, J. C.; Landau, U. Voltammetry Studies of Single-Crystal and Polycrystalline Diamond Electrodes. *J. Electrochem. Soc.* **1999**, *146* (8), 2959−2964.

(84) Enache, T. A.; Chiorcea-Paquim, A.-M.; Fatibello-Filho, O.; Oliveira-Brett, A. M. Hydroxyl radicals electrochemically generated in situ on a boron-doped diamond electrode. *Electrochem. Commun.* **2009**, *11* (7), 1342−1345.

(85) May, P. W.; Ludlow, W. J.; Hannaway, M.; Heard, P. J.; Smith, J. A.; Rosser, K. N. Raman and conductivity studies of boron-doped microcrystalline diamond, facetted nanocrystalline diamond and cauliflower diamond films. *Diamond Relat. Mater.* **2008**, *17* (2), 105−117.

(86) Mortet, V.; Vlčková Živcová, Z.; Taylor, A.; Frank, O.; Hubík, P.; Trémouilles, D.; Jomard, F.; Barjon, J.; Kavan, L. Insight into boron-doped diamond Raman spectra characteristic features. *Carbon* **2017**, *115*, 279−284.

(87) Bernard, M.; Baron, C.; Deneuville, A. About the origin of the low wave number structures of the Raman spectra of heavily boron doped diamond films. *Diamond Relat. Mater.* **2004**, *13* (4−8), 896−899.

(88) Yokoya, T.; Ikenaga, E.; Kobata, M.; Okazaki, H.; Kobayashi, K.; Takeuchi, A.; Awaji, A.; Takano, Y.; Nagao, M.; Sakaguchi, I.; Takenouchi, T.; Kobayashi, K.; Kawarada, H.; Oguchi, T. Core-level electronic structure evolution of heavily boron-doped superconducting diamond studied with hard x-ray photoemission spectroscopy. *Phys. Rev. B* **2007**, *75* (20), 205117.

(89) Hutton, L. A.; Iacobini, J. G.; Bitziou, E.; Channon, R. B.; Newton, M. E.; Macpherson, J. V. Examination of the Factors Affecting the Electrochemical Performance of Oxygen-Terminated Polycrystalline Boron-Doped Diamond Electrodes. *Anal. Chem.* **2013**, *85* (15), 7230−7240.

(90) Goeting, C. H.; Marken, F.; Gutiérrez-Sosa, A.; Compton, R. G.; Foord, J. S. Electrochemically induced surface modifications of boron-doped diamond electrodes: an X-ray photoelectron spectroscopy study. *Diamond Relat. Mater.* **2000**, *9* (3−6), 390−396.

(91) Denisenko, A.; Pietzka, C.; Romanyuk, A.; El-Hajj, H.; Kohn, E. The electronic surface barrier of boron-doped diamond by anodic oxidation. *J. Appl. Phys.* **2008**, *103* (1), 014904.

(92) Stumm, C.; Grau, S.; Speck, F. D.; Hilpert, F.; Briega-Martos, V.; Mayrhofer, K.; Cherevko, S.; Brummel, O.; Libuda, J. Reduction of Oxide Layers on Au(111): The Interplay between Reduction Rate, Dissolution, and Restructuring. *J. Phys. Chem. C* **2021**, *125* (41), 22698−22704.

(93) Jalalpoor, D.; Göhl, D.; Paciok, P.; Heggen, M.; Knossalla, J.; Radev, I.; Peinecke, V.; Weidenthaler, C.; Mayrhofer, K. J. J.; Ledendecker, M.; Schüth, F. The Impact of Antimony on the Performance of Antimony Doped Tin Oxide Supported Platinum for the Oxygen Reduction Reaction. *J. Electrochem. Soc.* **2021**, *168* (2), 024502.

(94) Weber, T.; Ortmann, T.; Escalera-López, D.; Abb, M. J. S.; Mogwitz, B.; Cherevko, S.; Rohnke, M.; Over, H. Visualizing Potential-Induced Pitting Corrosion of Ultrathin Single-Crystalline IrO2(110) Films on RuO2(110)/Ru(0001) under Electrochemical Water Splitting Conditions. *ChemCatChem* **2020**, *12* (3), 855−866.

(95) Weber, T.; Pfrommer, J.; Abb, M. J. S.; Herd, B.; Khalid, O.; Rohnke, M.; Lakner, P. H.; Evertsson, J.; Volkov, S.; Bertram, F.; Znaiguia, R.; Carla, F.; Vonk, V.; Lundgren, E.; Stierle, A.; Over, H. Potential-Induced Pitting Corrosion of an IrO2(110)-RuO2(110)/Ru(0001) Model Electrode under Oxygen Evolution Reaction Conditions. *ACS Catal.* **2019**, *9* (7), 6530−6539.

(96) Geiger, S. Stability investigations of iridium-based catalysts towards acidic water splitting. Ph.D. Thesis, Ruhr University Bochum, 2018. https://hss-opus.ub.rub.de/opus4/frontdoor/index/index/docId/5589.

(97) Vodeb, O.; Lončar, A.; Bele, M.; Hrnjić, A.; Jovanovič, P.; Gaberšček, M.; Hodnik, N. Intrinsic properties of nanoparticulate Ir-based catalysts for oxygen evolution reaction by AC voltammetry. *Electrochim. Acta* **2023**, *464*, 142882.

(98) Watzele, S.; Hauenstein, P.; Liang, Y.; Xue, S.; Fichtner, J.; Garlyyev, B.; Scieszka, D.; Claudel, F.; Maillard, F.; Bandarenka, A. S. Determination of Electroactive Surface Area of Ni-Co-Fe-and Ir-Based Oxide Electrocatalysts. *ACS Catal.* **2019**, *9* (10), 9222−9230.

(99) Lončar, A.; Jovanovič, P.; Hodnik, N.; Gaberšček, M. Determination of the Electroactive Surface Area of Supported Ir-Based Oxygen Evolution Catalysts by Impedance Spectroscopy: Observed Anomalies with Respect to Catalyst Loading. *J. Electrochem. Soc.* **2023**, *170* (4), 044504.

(100) Fathi Tovini, M.; Damjanovic, A. M.; El-Sayed, H. A.; Speder, J.; Eickes, C.; Suchsland, J.-P.; Ghielmi, A.; Gasteiger, H. A. Degradation Mechanism of an IrO2 Anode Co-Catalyst for Cell Voltage Reversal Mitigation under Transient Operation Conditions of a PEM Fuel Cell. *J. Electrochem. Soc.* **2021**, *168* (6), 064521.

(101) Pohl, M. D.; Haschke, S.; Göhl, D.; Kasian, O.; Bachmann, J.; Mayrhofer, K. J. J.; Katsounaros, I. Extension of the Rotating Disk Electrode Method to Thin Samples of Non-Disk Shape. *J. Electrochem. Soc.* **2019**, *166* (15), H791−H794.